Supersonic microwave plasma : potential and limitations for energy-efficient $[CO_2]$ conversion

Reference:

Vermeiren Vincent, Bogaerts Annemie.- Supersonic microw ave plasma : potential and limitations for energy-efficient $[CO_2]$ conversion
The journal of physical chemistry : C : nanomaterials and interfaces - ISSN 1932-7447 - 122:45(2018), p. 25869-25881
Full text (Publisher's DOI): https://doi.org/10.1021/ACS.JPCC.8B08498
To cite this reference: https://hdl.handle.net/10067/1554120151162165141

Supersonic Microwave Plasma: Potential and Limitations for Energy-Efficient CO_2 Conversion

Vincent Vermeiren and Annemie Bogaerts*

Department of Chemistry, Research group PLASMANT, University of Antwerp,
Universiteitsplein 1, 2610 Antwerp, Belgium

E-mail: annemie.bogaerts@uantwerpen.be

Abstract

Supersonic flows provide a high thermodynamic non-equilibrium, which is crucial for energy-efficient conversion of CO_2 in microwave plasmas, and are therefore of great interest. However, the effect of the flow on the chemical reactions is poorly understood. In this work, we present a combined flow and plasma chemical kinetics model of a microwave CO_2 plasma in a Laval nozzle setup. The effects of the flow field on the different dissociation and recombination mechanisms, the vibrational distribution, and the vibrational transfer mechanism are discussed. In addition, the effect of experimental parameters, like position of power deposition, outlet pressure, and specific energy input, on the CO_2 conversion and energy efficiency is examined. The short residence time of the gas in the plasma region, the shockwave, and the maximum critical heat, and thus power, that can be added to the flow to avoid thermal choking are the main obstacles to reaching high energy efficiencies.

Introduction

The threat of man-made climate change is one of the most prominent problems of the 21st century. A possible pathway to limit the scope of this problem is CO_2 capture. This process is cost intensive, both for capture from ambient air, as for capture from point sources,[1] resulting in extensive research in converting this waste product to value added chemicals.

Low-temperature plasmas are gaining increasing interest for the dissociation of CO_2 into CO, which can be combined with hydrogen gas to synthesize hydrocarbons. These plasmas are characterized by a high thermodynamic non-equilibrium between the electrons and the so-called heavy plasma species, allowing endothermic reactions to take place without heating the gas.[2] In particular, microwave plasmas show promising results for the energy-efficient conversion of CO_2.[2,3] This is attributed to the important role of vibrational induced dissociation.[2–6] Indeed, in microwave CO_2 plasmas, the relatively low electron temperature of about 1 eV allows for an efficient energy transfer from the electrons to the asymmetric mode vibrational levels of CO_2.[2] In excess of 90% of the electron energy is converted to vibrational energy.[7]

These vibrationally excited CO_2 molecules will exchange vibrational energy with other vibrationally excited molecules until they reach the dissociation limit, in a process called vibrational-vibrational (VV) relaxation.[2,4–6] This process is energetically more favourable than direct electron impact dissociation,[2] which is the main dissociation reaction in other plasma reactors, such as dielectric barrier discharges.[4,7,8] However, part of the vibrational energy is also converted to translational energy, or gas heating, in a process called vibrational-translational (VT) relaxation.[2,4–6] The key to higher energy efficiency is limiting the VT relaxation with respect to VV relaxation.

Berthelot and Bogaerts studied the effect of different discharge conditions on the energy efficiency and CO_2 conversion in microwave plasmas.[6] They concluded that lower pressures, higher power densities, lower temperature, and cooling of the afterglow had a beneficial effect on the efficiency of the dissociation process. The lower pressure and higher power densities lead to more vibrational excitation, which is beneficial for the conversion. A lower temperature results in more pronounced VV transfer with respect to VT transfer, while cooling of the afterglow limits the recombination of CO and O back to CO_2.

The requirement of low pressure and low temperature, however, poses challenges for industrial application of the technique. A microwave supersonic flow reactor can tackle these two issues, and has therefore demonstrated the maximum energy efficiency to date.[9] In this setup, a pressure difference is applied over a converging-diverging nozzle. The adiabatic expansion of the nozzle cross section accelerates the flow to supersonic velocities. A first benefit of this type of reactor is that the acceleration to supersonic speed creates a pressure drop, from high pressure conditions ($\geq$ 1 bar) to intermediate pressure (around 100 mbar), the latter being more beneficial for energy-efficient conversion.[2,6,10] A second benefit is that the rapid increase in kinetic energy reduces the internal energy of the gas, thus lowering the temperature.[11] This allows the use of higher power densities, while staying at low temperatures, which is also beneficial for energy-efficient CO_2 conversion.

Even in the absence of electromagnetic coupling, the supersonic flow field can drive the overpopulation of the highly excited vibrational states, leading to dissociation of CO_2.[2] This effect of supersonic expansion on the non-equilibrium vibrational distribution function in CO_2 was theoretically studied by Peerenboom et al.[12] in a quasi 1D model, which includes 21 asymmetric mode vibrational levels and state-to-state vibrational kinetics. The model shows that supersonic expansion indeed has a beneficial effect on the population of the highest vibrational levels.

In this paper, we present a combined supersonic flow model and chemical reaction kinetics model of a supersonic microwave CO_2 plasma in a converging-diverging nozzle geometry. The aim of this work is to study the effect of different characteristics of supersonic flow, e.g. pressure drop, and the shock wave, on the reaction kinetics. Based on this information, we will change the flow conditions in the model, in order to manipulate the flow field to examine the effect of the latter on the CO_2 conversion.

Computational Details

The study consists of two separate parts. First, non-reactive flow simulations are performed in COMSOL multiphysics. A 2D axisymetric high Mach flow number k/ϵ-model is used to calculate the flow for pure CO_2 at room temperature. This model combines the standard Reynolds Average Navier Stokes (RANS) k/ϵ-model with Euler's equations for inviscid flow, and will be explained in more detail in section . This model is chosen based upon its user-friendly nature, and the limited amount of computational resources and time needed to acquire results. Certain aspects of the flow behavior are not captured in our model in contrast to more complex simulations.[13] However, the effect of the approximations are not to an extent that will be relevant for this study.

Subsequently, a center cut line of the flow results is used as input in a zero-dimensional chemical kinetics model, described in more detail in section . The chemistry set that is used is presented in section . During the different simulations, the pressure and temperature will be fixed. The flow and plasma description are thus decoupled. The validity of this assumption, as well as other model approximations, will be discussed in more detail in section

Flow Model

The standard RANS k/ϵ-model is well known in computational fluid dynamics theory and can describe a wide range of turbulent flows.[14] It is a two-equation turbulence model that solves for the mass and momentum continuity partial differential equations:

$$\nabla . (\rho \vec{u}_g) = 0 \tag{1}$$

$$
\begin{aligned}
\rho\left(\vec{u}_g \cdot \nabla\right)\vec{u}_g = \nabla\Big[-p\vec{I} + \left(\mu+\mu_T\right)\left(\nabla\vec{u}_g + \nabla\left(\vec{u}_g\right)^T\right) \\
+\frac{2}{3}\left(\mu+\mu_T\right)\left(\nabla\cdot\vec{u}_g\right)\vec{I} - \frac{2}{3}\rho k\vec{I}\Big] + \vec{F}
\end{aligned}
\tag{2}
$$

where ρ stands for the gas density, $\vec{u}_g$ is the gas flow velocity vector, superscript T stands for transposition, p is the gas pressure, μ and μ_T are the dynamic and turbulent viscosity of the fluid, k is the turbulent kinetic energy, $\vec{I}$ is the unity tensor and $\vec{F}$ is the body force vector. Next to this, the turbulence is modelled by adding two additional equations that solves for the turbulent kinetic energy k, and the turbulent dissipation rate ϵ:

$$
\rho\left(\vec{u}_g \cdot \nabla\right)k = \nabla\cdot\left[\left(\mu+\frac{\mu_T}{\sigma_k}\right)\nabla k\right] + P_k - \rho\epsilon
\tag{3}
$$

$$
\rho\left(\vec{u}_g \cdot \nabla\right)\epsilon = \nabla\cdot\left[\left(\mu+\frac{\mu_T}{\sigma_\epsilon}\right)\nabla \epsilon\right] + C_{\epsilon 1}\frac{\epsilon}{k}P_k - C_{\epsilon 2}\rho\frac{\epsilon^2}{k}
\tag{4}
$$

Equation 3 and 4 calculate the transport of turbulent energy and its dissipation into heat (ϵ), respectively. P_k represents the production term for turbulent kinetic energy. σ_k, σ_ϵ, $C_{\epsilon 1}$, and $C_{\epsilon 2}$ are model constants which are experimentally determined.[14]

Since all flow properties are coupled to each other, the number and combinations of boundary conditions that are needed for well posedness depend on the flow state 15. In order to provide consistent inlet and outlet boundary conditions, the speed at which the different flow quantities propagate at the boundary needs to be known.

A plane wave analysis of the inviscid part of the flow is performed in order to apply a consistent number of boundary conditions, using the method described in detail in ref. 16. Inviscid flow is described by Euler's equations, which can be written as

$$
\frac{\partial\vec{Q}}{\partial t} + \frac{\partial\vec{F}_j}{\partial\vec{Q}}\frac{\partial\vec{Q}}{\partial x_j} = 0
\tag{5}
$$

where

$$\vec{Q} = \begin{bmatrix} \rho \\ u_i \\ p \end{bmatrix}$$

with $\vec{Q}$ the state vector to be solved for, $\vec{F_j}$ the flux vector and ρ, u_i and p the mass density, velocity components and pressure, respectively.

Plasma Model

The plasma chemistry is described with the ZDPlaskin code.[17] This model describes the time evolution of different plasma species in a non-equilibrium discharge. The time evolution of the different species through the reactor can be converted to an axial evolution through the discharge tube by calculating the velocity u of the considered volume element. Given the input values for pressure, temperature, and mass flow rate that were acquired from the flow model, the velocity is calculated from the conservation of mass flow rate

$$u = \frac{\dot{m}}{\rho A} \tag{6}$$

with $\dot{m}$ the mass flow rate, $\rho = \sum_j n_j Mj$ the mass density of the gas, and A the tube cross-sectional area, which is a function of the axial position, due to the converging-diverging nozzle. n_j is the number density of element j and M_j the mass of element j. The model starts at the inlet ($z = 0$) with pure CO_2. The plasma is assumed to be ignited at a certain axial position in the reactor. In the plasma region, two plasma parameters are fixed. The reduced electric field is fixed to a value of $50Td$, and the ionization degree to 10^{-6}, which are both typical values for CO_2 microwave plasmas.[3,10] A certain power deposition density $Q_{dep}(z)$ is applied in order to sustain the plasma with these values for electron density and energy. The total power input $P_{dep}(z) = \int_{z_0}^{z} A(z) Q_{dep} dz$ (with $A(z)$ the cross section of the tube at position z) is then used to calculate the specific energy input ($SEI[eV/molec.]$) at position z

$$SEI(z) = \frac{P_{dep}(z)}{\Phi}\frac{T_{ref}}{p_{ref}}\frac{k_B}{e}\frac{1}{10^{-3}} \tag{7}$$

where $\Phi[sls]$ is the gas flow rate in standard litres per second, $T_{ref} = 273.15\ K$ and $p_{ref} = 101325\ Pa$ are the temperature and pressure at standard conditions, e is the elementary charge to convert J into eV, and k_B is the Boltzmann constant. The factor 10^{-3} comes from the conversion of $l = dm^3$ to m^3. We use a fixed value for the SEI, and apply a power deposition until the value for the SEI is reached at $z = z_0 + z_p$, with z_p the plasma length, after which the power deposition drops to 0. This approach can be seen in figure 1, and was used in similar studies by our group.[18,19] The plasma length is calculated by the model, based on the SEI value used. This is preferable, since no experimental data are available on the plasma length in this type of reactor.

The microwave power is mainly absorbed by the electrons in the system due to their lower mass, and thus higher mobility. Given the importance of the electron energy distribution function (EEDF) to the chemistry, the model has a built-in Boltzmann solver BOLSIG+[20] that uses the two-term approximation to calculate EEDF, the electron kinetics and the energy dependent rate coefficients of the various electron impact reactions (Table 1 in SI), using the Phelps 7eV excitation cross section[21] recommended by Bogaerts et al.[22] The heavy particles are assumed to be in thermal equilibrium and are just described by the mean gas temperature T_g.

The Boltzmann solver is coupled to the chemical kinetics part of the model. In the latter part, the species densities n_s are calculated at every timestep by a set of conservation equations

$$\frac{dn_s}{dt} = \sum_j R_j[a^R_{sj} - a^L_{sj}] = \sum_j (k_j \prod_l n_l)[a^R_{sj} - a^L_{sj}] \tag{8}$$

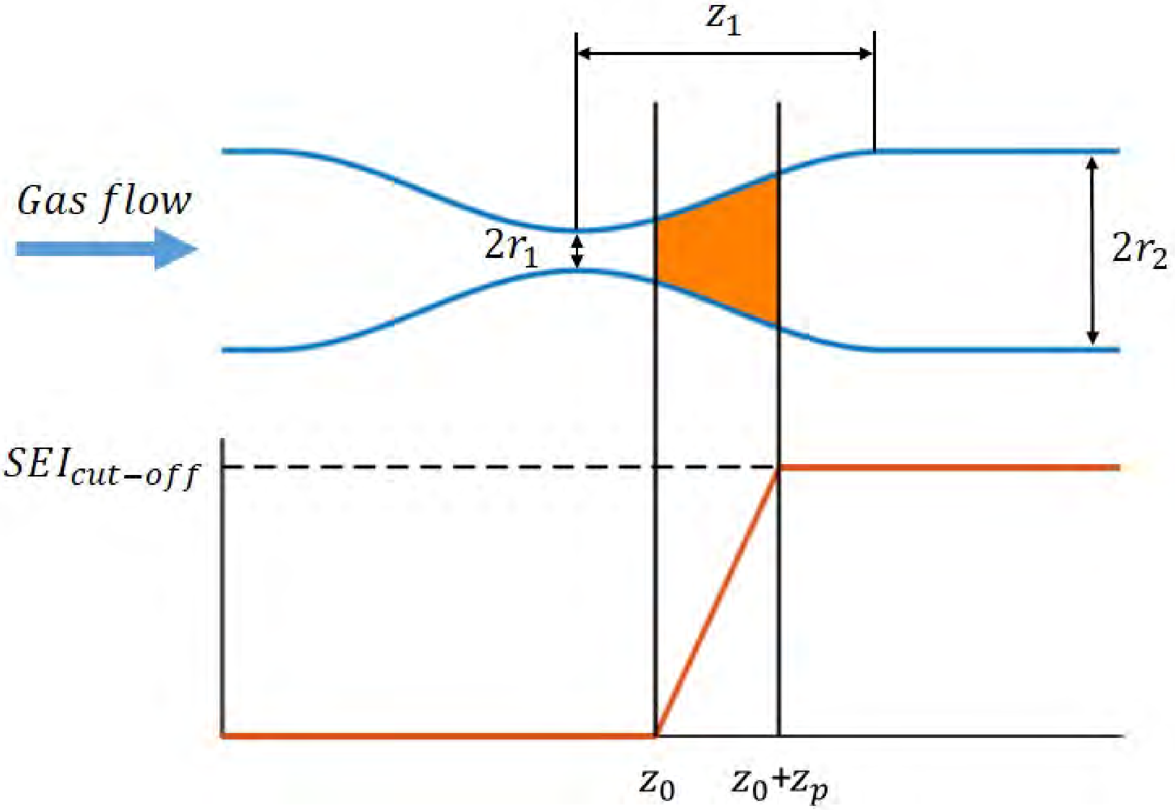

Figure 1: Schematic presentation of the Laval nozzle geometry (top) with plasma (orange) and specific energy input SEI (bottom) in function of the axial distance in the geometry. The plasma starts at z_0 and continues until the cut-off value for the SEI is reached at $z_0 + z_p$, with z_p the plasma length.

Index j refers to reaction j and index l refers to the different reactants of reaction j. a^R_{sj} and a^L_{sj} the right- and left-hand side stoichiometric coefficients of species s, respectively. k_j is the reaction rate coefficient of reaction j, with $R_j = k_j \prod_l n_l$ the reaction rate.

One of the main objectives of this study is to examine conditions for the highest CO_2 conversion and energy efficiency. The model calculates the conversion (χ) and energy efficiency (η) as follows

$$\chi(z) = 100 \times \left(1 - \frac{N_{CO_2}(z)v(z)A(z)}{N_{CO_2}(0)v(0)A(0)}\right) \tag{9}$$

$$\eta = \chi \frac{\Delta H^\circ}{SEI} \tag{10}$$

with N_{CO_2} the number density of CO_2, $v(z)$ the velocity of the volume element at position z, $A(z)$ the cross section of the discharge tube at position z, and ΔH° the enthalpy of the reaction $CO_2 \rightarrow CO + \frac{1}{2}O_2$.

Chemistry Set

Species

The chemistry set, used in this model, is based on the chemistry set reported in.[18,19] This set resulted from a chemistry reduction process,[23] initiated from the original set by Kozák and Bogaerts[4,5] that was later finetuned by Koelman et al.[24] In this reduction, the species of minor importance to the plasma chemistry were removed, which reduces the complexity, but also the uncertainty on the outcome of the model results.[18]

The species included in this model are listed in Table 1. The set includes 21 asymmetric mode vibrational levels $CO_2[v_{1-21}]$ up to the dissociation limit, as well as 4 symmetric mode levels $CO_2[v_{a-d}]$. For CO, 10 vibrational levels are included. The energy of the different CO_2 vibrational levels is calcuclated using formula (11), as in:[4,25]

$$E_{CO_2} = \sum_i \omega_i (v_i + \frac{d_i}{2}) + \sum_{j \geq i} x_{ij} (v_i + \frac{d_i}{2})(v_j + \frac{d_j}{2}) + x_{l_2 l_2} l_2^2 \tag{11}$$

in which ω_i, x_{ij} and $x_{l_2 l_2}$ are spectroscopic constants determined by experiments and d_i = $(d_1\ d_2\ d_3)$ = (1 2 1) are the degeneracies of the three modes of vibration. The values for the spectroscopic constants can be found in ref. 25: ω_1 = 1354.31 cm^{-1}, ω_2 = 672.85 cm^{-1}, ω_3 = 2396.32 cm^{-1}, x_{11} = -2.93 cm^{-1}, x_{12} = -4.61 cm^{-1}, x_{13} = -19.82 cm^{-1}, x_{22} = 1.35 cm^{-1}, x_{23} = -12.31 cm^{-1}, x_{33} = -12.47 cm^{-1}, $x_{l_2 l_2}$ = -0.97 cm^{-1}.

The energies of the CO vibrational levels are calculated using the anharmonic oscillator formula:[26]

$$E = \omega_e(v + 0.5) - \omega_e x_e(v + 0.5)^2 \tag{12}$$

where v is the vibrational quantum number, $\omega_e = 2169.81$ cm^{-1} and $x_e = 6.12 \times 10^{-3}$ is the anharmonicity coefficient. The values for these spectroscopic constants are taken from the NIST database.[27] The energies of the O_2 vibrational levels are taken from the Phelps database.[21]

Table 1: Species described in the model.

Neutral ground states
CO_2, CO, O_2, O, C

Charged species
CO_2^+, CO^+, CO_4^+, O^-, O_2^-, CO_3^-, CO_4^-, e^-

Excited states	Associated energy [eV]	State^a
$O_2[v_{1-4}]$	Anharmonic oscillator	
$CO[v_{1-10}]$	Anharmonic oscillator	
$CO_2[v_{1-21}]$	Anharmonic oscillator	(00n)
$CO_2[v_a]$	0.083	(010)
$CO_2[v_b]$	0.167	(020) + (100)
$CO_2[v_c]$	0.252	(030) + (110)
$CO_2[v_d]$	0.339	(040) + (120) + (200)
$CO_2[e_1]$	10.5	$(^1\Sigma_u^+) + (^3\Pi_u) + (^1\Pi_u)$
$O_2[e_1]$	0.98	$(a^1\Delta_g) + (b^1\Sigma_g^+)$
$O_2[e_2]$	8.4	$(B^3\Sigma_u^-)$ + higher triplet states
$CO[e_1]$	6.22	$(a^3\Pi_r)$
$CO[e_2]$	7.9	$(A^1\Pi)$
$CO[e_3]$	13.5	$(a'^3\Sigma^+) + (d^3\Delta_i) + (e^3\Sigma^-) + (b^3\Sigma^+)$
$CO[e_4]$	10.01	$(C^1\Sigma^+) + (E^1\Pi) + (B^1\Sigma^+) + (I^1\Sigma^-) + (D^1\Delta)$

[a] CO_2 electronic states designation from Grofulović et al.,[28] O_2 and CO electronic states notation from Huber & Herzberg.[29]

Reaction Kinetics

The reactions included in the model are listed in Supporting Information (SI). The electron impact reactions are shown in Table S1 and S2. The reactions of Table S1 are described by electron impact cross sections, found in the LXCat database,[30] while the reactions in Table S2 are described by rate coefficients, calculated with analytical expressions. Given that the cross sections for vibrational excitation are only available from ground state molecules to the lowest levels, the other cross sections for electron impact excitation between different vibrational levels are calculated using the Fridman approximation,[2] which is based on the semi-empirical formula:

$$\sigma_{nm}(\epsilon) = exp\left(\frac{\alpha(m-n-1)}{1+\beta n}\right)\sigma_{01}(\epsilon + E_{01} - E_{nm}) \tag{13}$$

in which $E_{01} = E_1 - E_0$ and $E_{nm} = E_m - E_n$ are the energy differences between vibrational states 1 and 0 and states m and n, respectively, ϵ is the electron energy, and the parameters $\alpha = 0.5$ and $\beta = 0$.[4,5] The neutral-neutral reactions are shown in Table S3. The rate coefficients are Arrhenius expressions.

$$k(T_g) = AT_g^B exp\left(\frac{E_a}{k_B T_g}\right) \tag{14}$$

where k is the rate coefficient, T_g the gas temperature, E_a the activation energy, and A and B are experimentally or theoretically determined constants. Molecules in vibrationally excited levels need lower energy to overcome the activation energy barrier. The efficiency of this lowering is described by the Fridman-Macheret approximative α model.[2] More information about the effect of this efficiency determining α parameter on the reaction mechanisms of microwave CO_2 plasmas can be found in ref. 19.

The rate coefficients for VV and VT transfer between different molecules can be found in Table S4. They are calculated by the Schwartz-Slawsky-Herzfeld (SSH) theory.[31] More information about the implementation of this SSH theory in the 0D model can be found in ref. 4.

Model Approximations

Every model needs approximations, so here we would like to point out the validity of the approximations made in this work. First, the setup is studied with a 0D model. This model is radially averaged and can thus not take into account any spatial gradients in the radial direction. In reality, a MW plasma can become contracted when operating at higher pressures,[32] which can thus not be captured by our model. A 0D model is however still favourable, since it yields a detailed description of the plasma chemistry, needed to evaluate the CO_2 conversion and energy efficiency, within limited calculation time.

Further approximations are related to the temperature of the molecules. When a supersonic flow expands, internal energy is converted to kinetic energy in order to fuel the acceleration.[11,33,34] This acceleration happens adiabatically if no heat source is applied on the flow. The flow is then described by the isentropic flow relations between pressure, temperature and density for a perfect gas:

$$\frac{p}{p_t} = \left(\frac{\rho}{\rho_t}\right)^{\gamma} = \left(\frac{T}{T_t}\right)^{\frac{\gamma}{\gamma-1}} = \left(1 + \frac{\gamma-1}{2}M^2\right)^{-\frac{\gamma}{\gamma-1}} \tag{15}$$

where p, T, ρ are the static pressure, temperature, and mass density, respectively, and p_t, T_t, ρ_t the total pressure, temperature and mass density, $\gamma = C_p/C_v$ is the ratio of specific heats, and M the Mach number of the flow. The total pressure, mass density and temperature are those when the flow is isentropically brought to rest, i.e. when $M = 0$, and are assumed to stay constant when no heat is exchanged with the environment.

Given that the flow and the plasma are decoupled, the effect of the plasma on the flow is not included in this model. When a plasma is created in the supersonic region, the applied electrical energy can either dissociate the gas, or can be lost in gas heating. Gas expansion due to conversion and rising temperature can lead to an increase in the molar flow rate. In this paper, however, the conversion is limited to a few percent (see section)), so the effect of the conversion on the flow will be low.

When heat is added to supersonic flow, the trends of the different physical parameters are quite different with respect to subsonic flow. Contrary to subsonic flow, heat addition in supersonic flows will lead to a deceleration of the flow to lower Mach numbers.[34] Such flow with heat addition is called Rayleigh-line flow[34] and is described by a Rayleigh curve. The added heat will lead to both a temperature and pressure increase.[34] This phenomenon is very unfavourable for MW plasma-based CO_2 conversion.[6] The amount of heat can increase until a critical value for added heat is reached. At that point, the gas is decelerated to $M \approx 1$, after which the flow will be thermally choked,[2,33,35,36] and a shock is generated. The critical heat (Q_{cr}) that can be added to a system, and still avoid thermal choking of the flow, can be estimated by the formula:

$$Q_{cr} = c_p T_0 \left[\frac{(M^2-1)^2}{2(\gamma+1)M^2[1+(1/2)(\gamma-1)M^2]} \right] \tag{16}$$

with c_p the specific heat capacity, and T_0 the inlet nozzle gas temperature. The critical heat can be augmented by an increase of the inlet nozzle temperature T_0 or by reagents dilution in noble gasses.[36]

Eq. 16 is valid for constant area ducts. The deceleration of the flow, due to heat addition, can be countered by increasing the cross-sectional area of the discharge over the region in which the heat is added.[36] This phenomenon is called 'nozzle profiling' and can double the critical heat with a sixfold increase of the cross-sectional area.[36] However, since the 0D model does not take into account radial contraction of the plasma, the plasma length is shorter than it would be in a full 3D (or 2D cylindrically symmetric) calculation. Hence, the plasma length is only a few millimetres long (see section). The formula of the constant area duct (eq. 16) can thus serve as a good estimate for our case, since a significant increase of the cross-sectional area over this distance is too complex and maybe impossible.

Figure 2 shows the critical heat as a function of Mach number. We can see that the critical heat rises with higher Mach numbers, until a maximum value of 0.1867 eV/molec. is reached at Mach ∞.

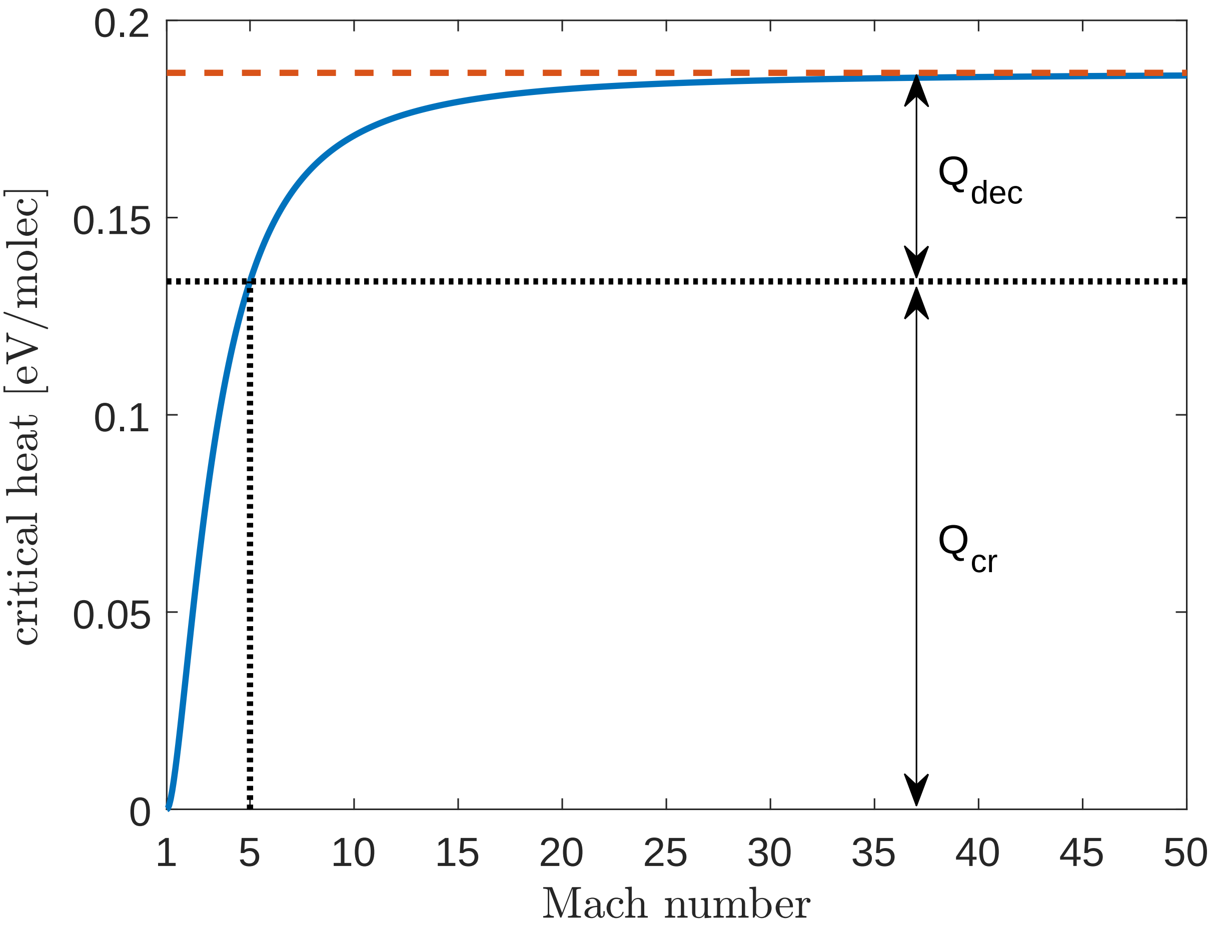

Figure 2: Critical heat before thermal choking of the flow occurs, as a function of Mach number (full line). With the maximum critical heat at high Mach numbers (dashed line) and the critical heat and the deceleration heat for an example at Mach = 5 (dotted line)

The heat that is added to the system, by the plasma, is $Q = (1-\eta) \times SEI$. This heat will increase the total temperature, while the total pressure is unaffected. The static pressure and temperature will increase (i.e. closer to the total values) due to the deceleration of the Mach number (see eq. 15). In this study, we use non-reactive flow results from COMSOL (i.e. without plasma) as input in a 0D plasma model. This means that the pressure and temperature remain fixed in the 0D model. Given that the total temperature (i.e. when the flow is at M = 0) remains at room temperature, we can assume that the reported energy efficiencies are maximum values of what can be achieved with this model, given that heat from the plasma would increase the total and static temperature and thus lower the energy efficiency.[6] To make sure that after the plasma is applied, the static temperature and pressure conditions are still valid, we will assume that the heat from the plasma has decelerated a hypothetical initial flow with much higher Mach number to the one which we are using. The maximum deceleration heat for a certain Mach number can then be defined by:

$$Q_{dec}(M) = Q_{cr}(M_{\infty}) - Q_{cr}(M) \tag{17}$$

where the flow decelerates from Mach ∞ to the Mach number from the flow results. For example, if flow conditions are used in which the Mach number reaches 5, then the maximum heat that can be added is the heat that slowed the flow down from Mach ∞ to Mach 5, i.e. $Q_{dec}(5) = Q_{cr}(M_{\infty}) - Q_{cr}(5) = 0.1867 - 0.1338 = 0.0529\ eV/molec.$. The maximum deceleration heat, and the critical heat are displayed in figure 2 for the example of Mach = 5. In this study, we make sure that the SEI is always chosen as not to violate the criterion of eq. 17. As mentioned above, the rising gas temperature due to the plasma can increase the molar flow rate. This effect is not taken into account in our flow model, because the plasma and flow model are decoupled. The magnitude of this effect is unclear and will depend on the specific energy input and the energy efficiency of the conversion process. We plan to study this effect in our future work, for which we will need to develop a fully coupled model.

Given that microwave CO_2 plasmas are characterized by their high thermodynamic non-equilibrium, the effect of the supersonic flow on the rotational and vibrational temperature needs to be discussed. In this study, the rotational degrees of freedom are assumed to be in equilibrium with translation, and will not be separately described. This assumption is valid for microwave CO_2 plasmas[37] since the rotational-translational relaxation only slows down at high gas temperatures.[38] We assume in this study that the vibrational temperature is also not affected by the supersonic expansion. Given that most of the energy for supersonic acceleration comes from translational energy, yielding a drop in gas temperature while the vibrational temperature remains constant, the non-equilibrium between these two is enhanced, leading to overpopulation of the vibrational levels with respect to the Boltzmann distribution.[2,12] This assumption is also used in vibrational collision studies of hypersonic flows[39,40]

Results and Discussion

In section , we will illustrate the flow field results without plasma, i.e., for pure CO_2 at room temperature inlet conditions. In section and , we will describe the evolution of the plasma through the reactor, with focus on the CO_2 dissociation and recombination mechanisms, and the evolution of the vibrational distribution function. In sections , , and , we will discuss in more detail the effect of plasma position, flow conditions, and power, on the overall energy efficiency and CO_2 conversion. Finally, in section , we will study the maximum theoretical energy efficiency for different inlet and outlet pressures.

Flow Field Results without Plasma

The three parameters that define the geometry (see figure 1) are chosen to resemble the dimensions in which high energy efficiency is reported:[9] $r_1 = 0.4$ cm, $r_2 = 2$ cm, and $z_1 = 10$ cm. The inlet nozzle is slightly larger than reported in.[9] The flow results for an inlet pressure $p_{in} = 2$ bar and outlet pressure $p_{out} = 1$ bar are plotted in figure 3, illustrating the axial velocity profile, the Mach number, the static pressure and the static temperature. The results are only shown in the expansion region of the nozzle, where the supersonic acceleration affects these quantities. We discuss here one flow field case, for one geometry, inlet and outlet pressure, in detail, but additional flow results for different conditions and geometries (i.e. different values for z_1) can be found in the SI.

The flow field consists of two distinct regions (depicted in figure 3(a)). First, the flow accelerates due to the nozzle expansion (region I), from an axial velocity of 6 m/s before the nozzle to 415 m/s (Figure 3(a)). This corresponds to a Mach number of 1.9 (Figure

3(b)). The static pressure exhibits a drop from 2 bar to 0.3 bar (Figure 3(c)), while the static temperature drops from 300 K to 187 K (Figure 3(d)).

The supersonic region I is followed by a discontinuous deceleration to sonic conditions, called a shock wave. This is characterized by a decrease in Mach number, and an increase in pressure and temperature. At the inlet pressure of 2 bar, the flow shows a single shock with bifurcated ends.[41,42] This shape is a result of boundary layer separation.[41] When the flow accelerates to a lower Mach number, the shock wave could exhibit a more curved shape.[41]

The shock wave separates the supersonic region from the mixing region (region II in figure 3(a)). In this region the pressure increases monotonically to the outlet pressure of 1 bar. The same trend is observed in the axial velocity, Mach number, and temperature, where a gradual return to sonic conditions takes place.

It can be seen in figure 3(a) that a part of the axial velocity (close to the walls) is negative. There is indeed a small portion of the flow that recirculates along the walls, after the shock wave. This effect can not be taken into account in a 0D model, but is of no importance, given that the ideal plasma location lies in the supersonic region, before the shockwave.

When the flow in the supersonic region accelerates to higher Mach numbers, a third region forms between the supersonic region and the mixing region, called the shock train. The shock train is characterized by a sequence of shocks separating subsonic from supersonic regions.[41] After each shock, the flow accelerates again to supersonic velocities, after which it is decelerated by the following shock. The region is characterized by pressure and temperature oscillations. This can be seen in figure S1 of the SI (region III), for an inlet pressure of p_{in} = 4 bar and outlet pressure of p_{out} = 1 bar, in which the flow accelerates to Mach 2.5. We want to note that in this case, the calculated minimum temperature of 141K is far below the desublimation point of CO_2 at the corresponding pressure of 0.2 bar, which is about 180 K.[43] In reality, cluster formation can occur in supersonic flow.[44] When a plasma is applied, the temperature will most likely stay above this desublimation point, so including this phenomenon in our model is not relevant for this study.

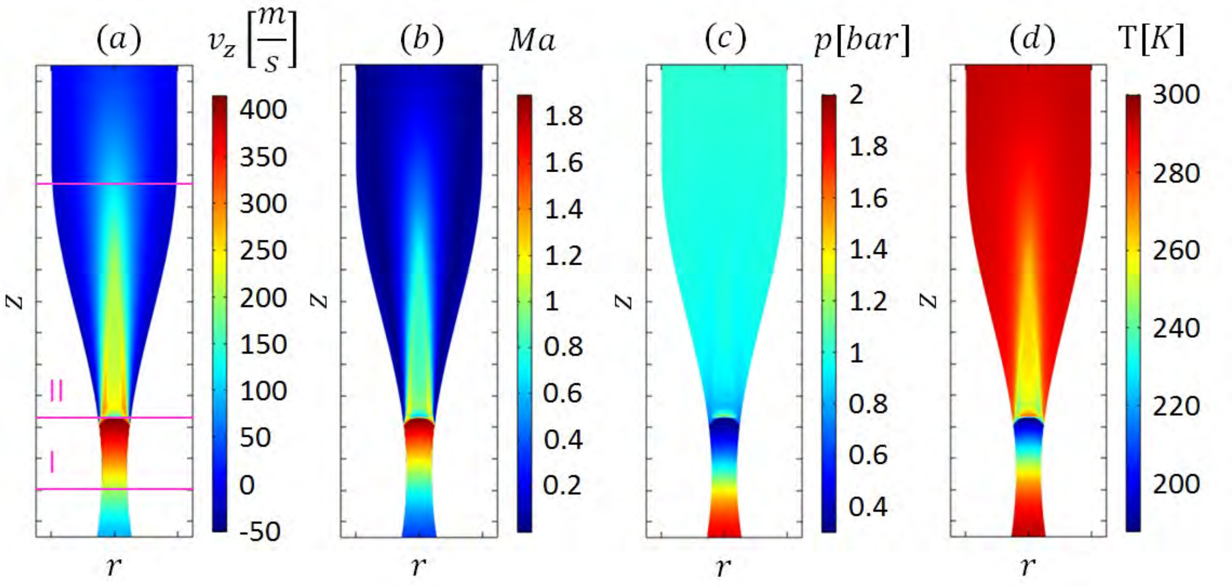

Figure 3: (a) Axial velocity magnitude (b) Mach number (c) static pressure and (d) static temperature in the case of $r_1 = 0.4$ cm, $r_2 = 2$ cm, $z_1 = 10$ cm, $p_{in} = 2$ bar, $p_{out} = 1$ bar.

Main CO_2 Dissociation and Recombination Mechanisms in the Plasma and Afterglow Region

The mechanisms will be studied by looking at the so-called reduced reaction rates of the different processes(i.e., $100 \times R/N[\%/s]$, with R and N the reaction rates and the total gas density, respectively). This approach is chosen to take into account the change of total density through the reactor. The results can hence be interpreted as the percentage of CO_2 that is converted or recombined through these processes, with 100 $\%/s$ meaning that all CO_2 is converted in 1 second. Note that the values exceed far beyond 100 $\%/s$, since the residence time is in the order of μs.

Figure 4 (top) shows the main dissociation and recombination mechanisms, when applying a SEI of 0.2 $eV/molec.$, in the supersonic flow region of a flow case with $p_{in} = 2$ bar and $p_{out} = 1$ bar, rendering M ≈ 1.9. The pressure variation as a function of position is illustrated in figure 4 (bottom). The plasma covers a domain of 1 mm (see purple rectangle in Figure 4), which corresponds to a residence time of 2.7 μs. The three main CO_2 dissociation mechanisms are electron impact dissociation (X4, blue curve), dissociation of ground-state and vibrationally excited CO_2 by collision with any molecule M (N1, red curve) and by reaction with an O radical (N2, yellow curve). The main recombination mechanism is recombination of CO with an O radical (N4, purple dotted curve).

At the start of the plasma, electron impact dissociation is the most prominent dissociation reaction. The reaction continues to be relevant in the entire plasma region, because of the abundance of free electrons, and drops to 0 at the end of the plasma. Vibrationally induced dissociation upon collision with any molecule (N1) becomes the most important dissociation mechanism at about 1/3 of the plasma length. The reason is that some time is required for the vibrational energy of CO_2 to climb the ladder up to the higher levels, from which dissociation can more easily take place. Given the high velocity, the gas travels some distance before this reaction becomes important. The same applies to dissociation by recombination with an O radical (N2), which even lags a little behind, since the O radicals first need to be produced by reaction (N1). At the same time, when the conversion rises in the plasma, recombination also becomes active, although the rate is much lower than for the dissociation reactions, given the low gas temperature.

As it takes some time for vibrationally induced dissociation to become a more active dissociation pathway, it is clear from these results that the short residence time (i.e. 2.7 μs) is also a limiting factor at this low SEI value. Indeed, after the high vibrational levels become more populated, the dissociation has little time to occur through this energetically favourable pathway. However, this could also be a result of working with a 0D model. In reality, radial contraction can increase the axial plasma length and thus the residence time, which would result in a greater importance of vibrationally induced dissociation, with respect to electron impact dissociation, in the plasma. At this stage, it is not possible to quantify this effect, but we plan to investigate this in the future, when developing a full 2D model. Furthermore, the residence time would also increase if the E/N (now set to 50 Td) or the ionization degree (now set to 10^{-6}) were lower. While reducing the ionization degree will have a negative impact on the energy efficiency, a reduction of the E/N has a positive impact.[19] However, values of 50 Td are characteristic for MW plasmas.[3]

In the afterglow, reactions N1 and N2 remain active, but the latter becomes the most dominant dissociation reaction. Both reactions are, however, quenched when the pressure increases in the shockwave region (between the lines at 19.22 cm and 19.36 cm). The most important recombination reaction (N4) shows an opposite trend. The reduced rate of this reaction remains the same in the afterglow, compared to the end of the plasma, but exhibits a pronounced rise in the shockwave region. After the shockwave, this reaction becomes more important than the dissociation reactions, which will limit the overall CO_2 conversion and energy efficiency.

Vibrational Distribution Function

In order to better understand the results of the previous section, we take a closer look at the evolution of the vibrational distribution function (VDF); see figure 5, for the same conditions as in figure 4. The three upper panels show VDFs, calculated at different axial positions, as indicated by the corresponding numbers in the plot of the pressure in the lower panel. At the plasma onset, the VDF shows no significant overpopulation of the vibrational levels, and is close to a Boltzmann distribution (no. 1). The vibrational temperature at that point is 237 K, while the gas temperature is 198 K. Since the supersonic acceleration increases the non-equilibrium between the gas temperature and the vibrational temperature, the value of the latter is slightly higher.[12] Very quickly, however, the vibrational levels get populated (no. 2-3), until the VDF reaches a stationary distribution (no. 4-7). This evolution explains the spatial delay in the rates of reactions N1 and N2, as displayed in figure 4. In the afterglow the VDF retains a high population of the higher vibrational levels (no. 8-10). However, in the shockwave, the pressure increases sharply from 305 mbar to about 1.15 bar over a distance of 1.4 mm, and the higher vibrational levels are depopulated (no. 11-14) due to VT relaxation and VV ladder downclimbing (see below). Right after the shockwave, the vibrational temperature is still high (1520 K). However, since the higher vibrational levels,

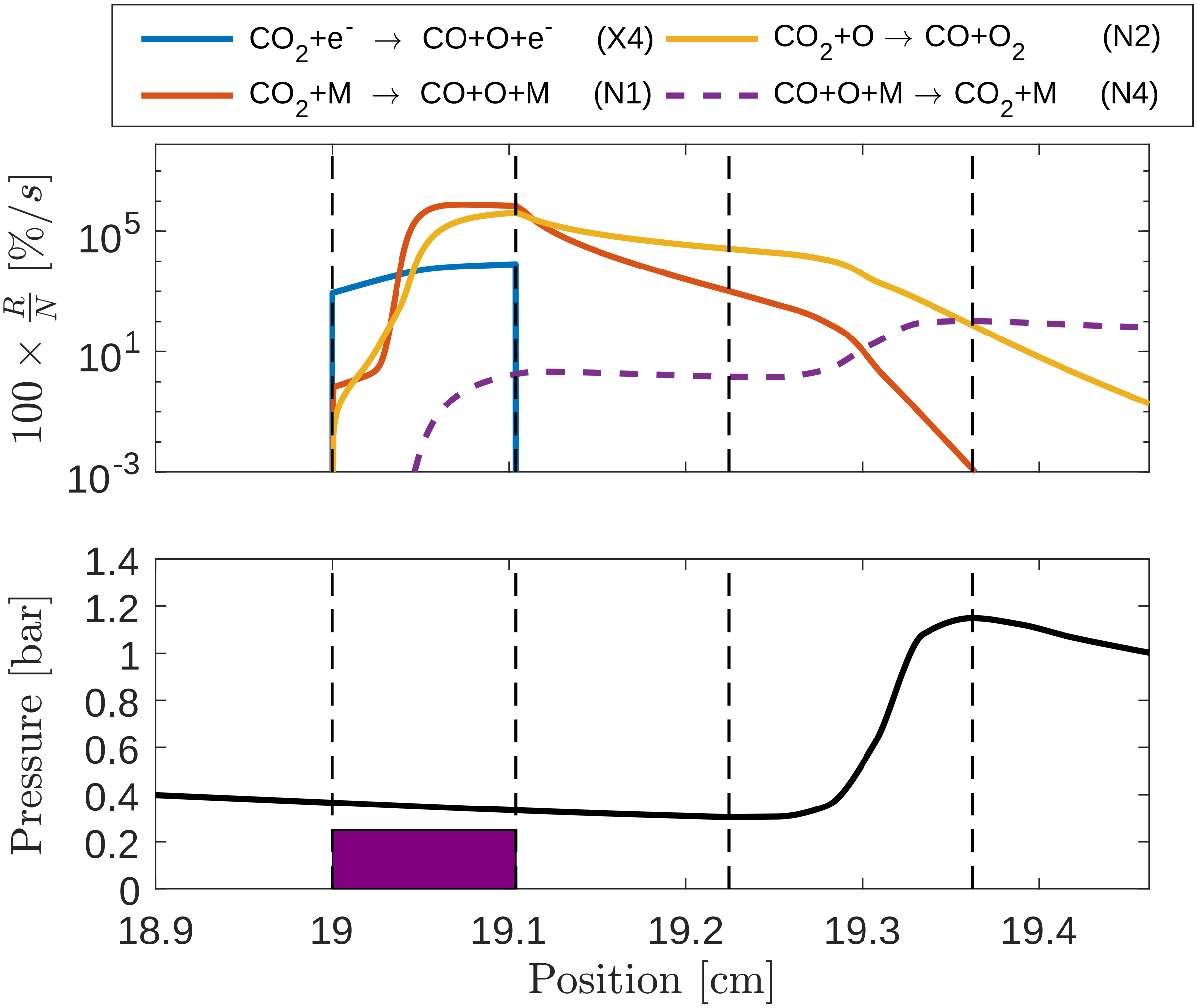

Figure 4: Top: Evolution of the main CO_2 dissociation and recombination mechanisms in the plasma and afterglow for the following conditions: SEI = 0.2 eV/molec., p_{in} = 2 bar, p_{out} = 1 bar, and geometry dimensions: r_1 = 0.4 cm, r_2 = 2 cm, z_1 = 10 cm. Bottom: Absolute pressure as a function of axial position with the plasma indicated as a purple rectangle.

from which dissociation occurs, are depopulated by VT relaxation and VV downclimbing, there is no more CO_2 dissociation at that position.

To understand what happens with the vibrational energy, we take a look at the main vibrational reaction mechanisms, namely VV and VT relaxation.

Figure 6 shows the density averaged reaction rate for electron impact vibrational excitation (eV), VV relaxation (VV) and VT relaxation (VT), multiplied with the energy transfer of the different processes. For eV en VV (top panel), it can be interpreted as the energy

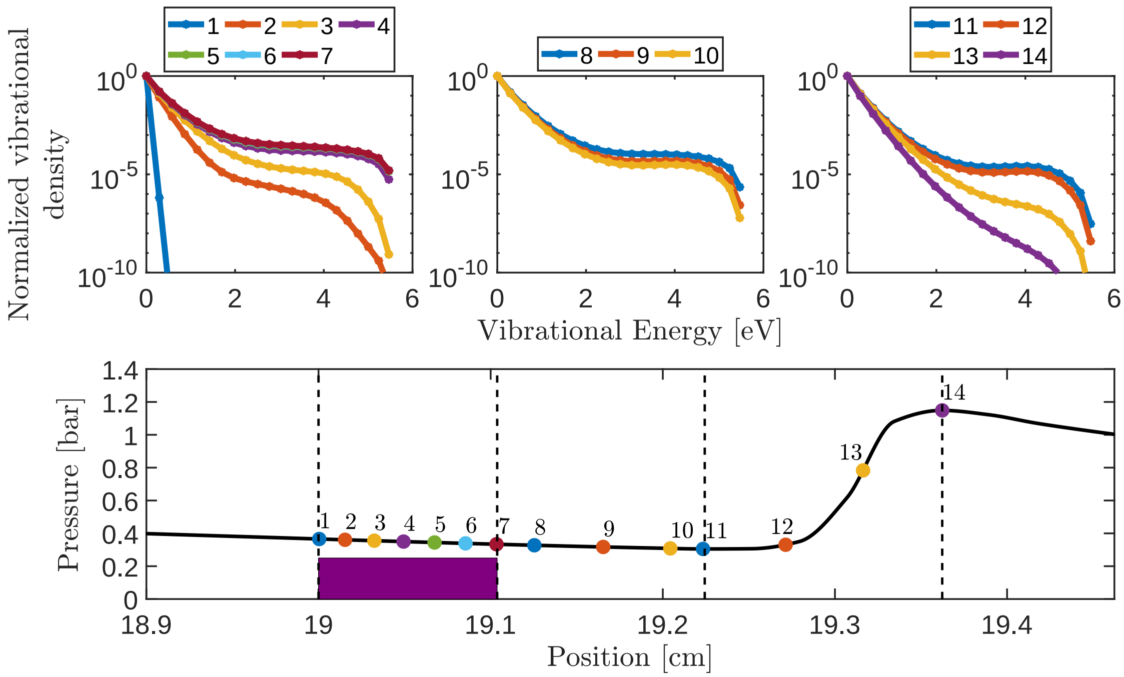

Figure 5: Evolution of the vibrational distribution function (VDF) for different axial positions as indicated on the pressure evolution in the lower panel, for the following conditions: SEI = 0.2 eV/molec., p_{in} = 2 bar, p_{out} = 1 bar, and geometry dimensions: r_1 = 0.4 cm, r_2 = 2 cm, z_1 = 10 cm.

that is transported up minus the energy transported down the vibrational ladder per second. For VT relaxation (middle panel) it is the energy lost to heat per second. This approach is chosen to give more weight to reactions with higher energy gains or losses.

To realize efficient vibrationally induced dissociation, the higher vibrational levels must be very quickly populated. At the start of the plasma, electron impact vibrational excitation is the only process that transports energy up the vibrational ladder (see figure 6, top panel). This process continues to transport energy up the vibrational ladder in the rest of the plasma. In the afterglow, this process obviously does not occur anymore. Initially, VV relaxation transports energy from the higher vibrational levels to lower vibrational levels in a ladder downclimbing process (see figure 6, top panel). This can be explained since most of the net energy from electron impact vibrational excitation goes to the second and third levels, and is partially returned to the first level in a ladder downclimbing process. This happens until the lower levels are sufficiently populated, and a stationary VDF is reached. More information about this can be found in the SI (Figures S2 and S3). In the second half of the plasma region, there is VV ladder climbing to the higher vibrational levels. This is continued in the afterglow, but the energy transported up the ladder gradually decreases, and reverses at some point (19.25 cm), so there is ladder downclimbing through the shockwave region.

The main vibrational energy loss, namely VT relaxation, rises in the plasma region (see figure 6, middle panel), due to the increasing vibrational overpopulation (cf. figure 5). In the afterglow, the VT energy loss slightly drops, but in the shockwave region, it rises again due to the rising pressure and temperature (see figure 3 above).

It is clear that the depopulation of the higher vibrational levels, as shown in figure 5, is the result of VV ladder downclimbing and increased VT relaxation.

Effect of Plasma Position on the CO_2 Conversion and Energy Efficiency

In the above results, the plasma was exactly located in the supersonic region. In this section, we will explore how changing the plasma position, by moving the position of the waveguide in the supersonic flow reactor, will affect the CO_2 conversion and corresponding energy efficiency. In figure 7 (top panel), we indicate different starting positions of the plasma region, keeping a fixed total SEI of 0.2 eV/molec. in a supersonic flow reactor with $r_1 = 0.4$ cm, $r_2 = 2$ cm, $z_1 = 10$ cm, at an inlet pressure of 2 bar and an outlet pressure of 1 bar (i.e., the same as in previous sections). In addition, the pressure evolution is shown. Note that the plasma lengths in the reactor are different, depending on the starting position, to keep the same SEI. While a larger reactor radius will result in a shorter axial plasma length, the plasma length seems more correlated with the pressure at which the plasma is ignited. Indeed, when the pressure is higher, the plasma length is shorter. This is a result of the higher power density applied to ignite a plasma with an ionization degree of 10^{-6}. In reality, axial and radial contraction of the plasma is observed at higher pressures,[45] but so far this has not been studied in CO_2 microwave plasmas.

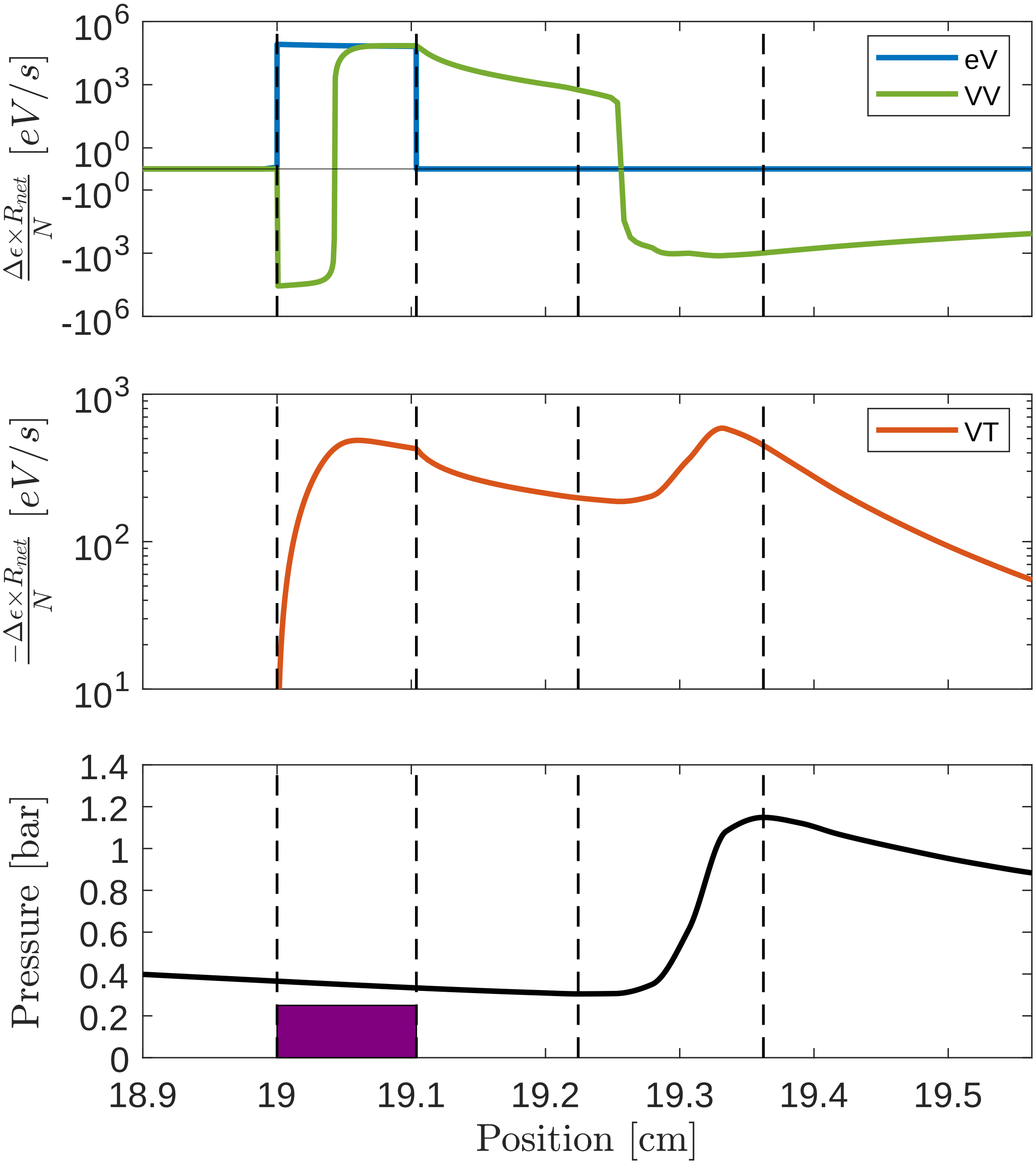

Figure 6: Evolution of electron impact vibrational excitation (eV, top panel), the VV relaxation (VV, top panel) and VT relaxation (VT, middle panel) through the plasma and afterglow, for the following conditions: SEI = 0.2 eV/molec., $p_{in} = 2$ bar, $p_{out} = 1$ bar, and geometry dimensions: $r_1 = 0.4$ cm, $r_2 = 2$ cm, $z_1 = 10$ cm. Bottom panel: Absolute pressure as a function of axial position with the plasma in purple rectangle.

Figure 7 (bottom panel) shows the energy efficiency (left axis) and CO_2 conversion (right axis) for the different plasma positions, displayed in the top panel. The most energetically favourable position is coloured in green in the top panel. The energy efficiency increases from 20.5 % to 26.5 % when moving deeper into the supersonic region. The conversion rises accordingly from 1.4 % to 1.8 %. Note that the calculated energy efficiency and conversion are proportional to each other, as the SEI is kept constant here (see eq. 10 above).

It can be seen that the most energetically favourable position (top panel) does not lie closest to the shockwave, where the pressure reaches its minimum. In fact, the energy efficiency is more than 1 % lower when the plasma lies directly in front of the shockwave. This is the result of the vibrational quenching effect due to the rising pressure in the shockwave (cf. figure 5 above), and the increasing importance of recombination, with respect to CO_2 dissociation (cf. figure 4 above). In contrast, when the plasma is generated somewhat before the shockwave, the dissociation reactions (N1, N2) continue to be important right after the plasma before the shockwave (see figure 4), and this has a beneficial effect on the overall conversion and energy efficiency.

Note that the results for energy efficiency and conversion were calculated in all cases with a fixed temperature profile, as obtained from the flow simulations (cf. figure 3). When the temperature would be calculated self-consistently, the energy efficiency and conversion, displayed in figure 7, would be somewhat lower.

Effect of Flow Conditions on the CO_2 Conversion and Energy Efficiency

With a fixed geometry, the main parameters that can be modified to change the flow field are the inlet and outlet pressure. Their effect on the flow field parameters can be seen in detail in the SI (Figures S5 and S6). Increasing the inlet pressure from 1 to 2 bar results in a lower temperature, a higher Mach number, and a lower minimum pressure. However, when the inlet pressure rises above 2 bar, the minimum pressure stays about the same, while the

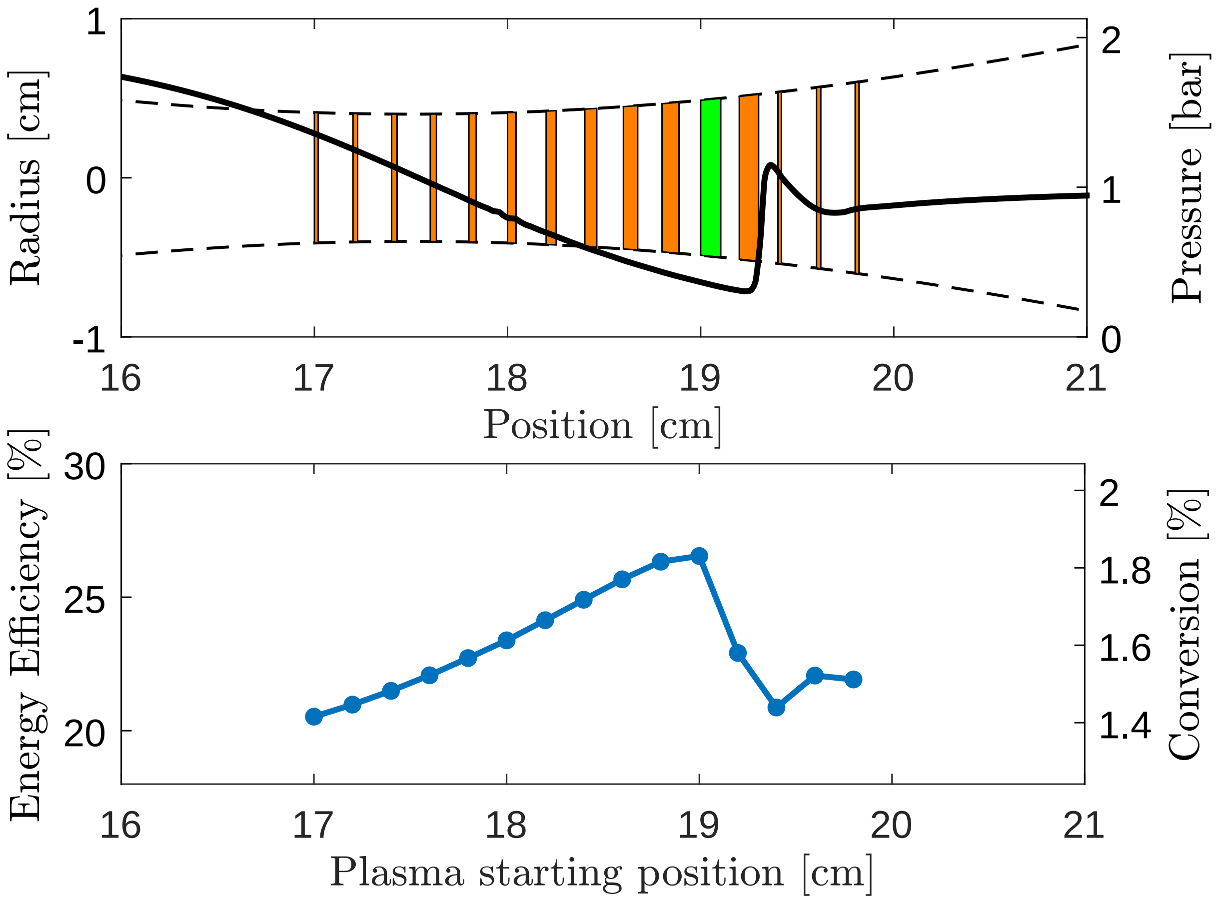

Figure 7: Top figure: Illustration of different plasma positions and plasma lengths as a function of the position in the reactor (dotted line), for which the CO_2 conversion and energy efficiency are calculated. Also shown is the pressure as a function of position in the reactor (full line). Bottom figure: Calculated energy efficiency and conversion for the different plasma positions indicated in the top figure.

temperature keeps decreasing and the Mach number keeps increasing.

Reducing the outlet pressure also yields a higher maximum velocity, a higher Mach number, a lower minimum temperature, and in addition, the minimum pressure drops, in contrast to a rise in inlet pressure where the drop in minimum pressure stops at inlet pressures above 2 bar. For energy-efficient CO_2 conversion, the outlet pressure is thus an ideal parameter to tune the flow field to reach optimum conditions. In this way, the negative effects of plasma heating due to the deceleration, namely an increase in temperature and pressure (see section), can be countered. An increase in inlet pressure would not have the same desired effect, since the total pressure is increased, and a similar increase in added heat (and subsequent decrease in Mach number) would result in a faster rise of the absolute pressure in the pressure drop (see equation 15). This means that the inlet pressure is not an ideal parameter to tune the flow in order to counter the effect of increasing pressure, and will hence not be described in this section. The maximum energy efficiencies that can be reached when changing this parameter will, however, be studied in more detail in section .

Here, we present the effect of the flow fields on the CO_2 conversion and energy efficiency, by varying the outlet pressure. Since a lower outlet pressure will increase the Mach number of the flow (see SI), and in order to stay consistent with the upper limit of the added heat (see eq. 17) we perform this study with a SEI of 0.15 eV/molec instead of 0.2 eV/molec.

Figure 8 shows the energy efficiency and conversion as a function of plasma position in the reactor, for three different outlet pressures (bottom panel). The pressure variation in these three cases is illustrated in the top panel. When the outlet pressure drops from 1 to 0.4 bar, the maximum energy efficiency increases from 20.46 % to 23.84 % (see bottom panel). When the outlet pressure is 1 bar, the minimum pressure is 307 mbar. The optimal plasma position for energy-efficient CO_2 conversion is then found between 19 cm (at a pressure of 365 mbar) and 19.08 cm (at a pressure of 342 mbar). When the outlet pressure is at 0.4 bar, the minimum pressure is 77 mbar. In this case, however, the highest energy efficiency is reached when the plasma is located between 19.8 cm (at a pressure of 180 mbar) and 19.95 cm (at a pressure of 158 mbar), hence much earlier than the shock wave position, compared to the case with outlet pressure of 1 bar. The reason is that the pressure for highest energy efficiency was found at pressures between 100 and 300 mbar.[2,6,10] Closer to the shockwave, where the minimum pressure of 77 mbar is reached, the energy efficiency is only 14.8%.

Effect of Power on the CO_2 Conversion and Energy Efficiency

When a high amount of heat is applied on a supersonic region, the flow needs to accelerate to higher Mach numbers, to avoid thermal choking of the flow (see figure 2). For that reason, it is interesting to study the effect of power on the dissociation pathways and the

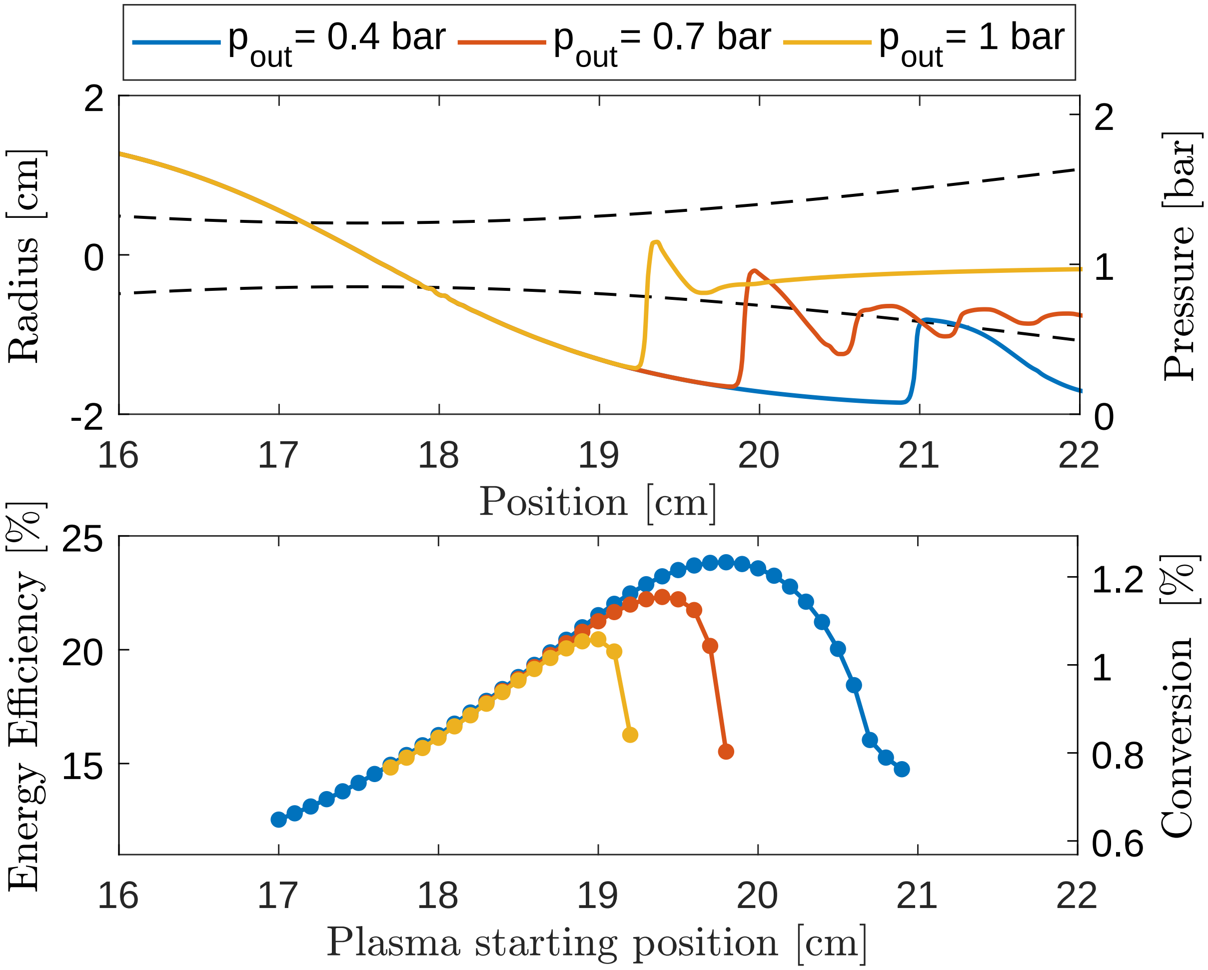

Figure 8: Top figure: Pressure distributions for three different values of outlet pressure (colored lines) as a function of position in the reactor (dotted lines). Bottom figure: Energy efficiency and CO_2 conversion as a function of the plasma position, for the same three different values of outlet pressure as in the top figure.

energy efficiency, since a lower amount of heat is then added to the flow, avoiding the initial acceleration to high Mach numbers. In this section, we will study these pathways for SEI of 0.05, 0.1, 0.15, and 0.2 eV/molec. We will not study the effect of higher SEI values, to avoid violating the maximum deceleration heat criterion (see eq. 17). The energy efficiency and CO_2 conversion as a function of plasma starting position for the above mentioned SEI values are included in the SI (Figure S4). They show the same trends as presented in section . The values for the maximum energy efficiency are 0.06 %, 9.4 %, 20.52, and % 26.5 %, respectively. The maximum energy efficiency thus increases much faster than the SEI (or input power). It should be noted that at higher SEI, a higher amount of heat is added to the flow, in spite of the higher energy efficiency. Indeed, $Q = (1 - \eta) \times SEI$ is 0.05, 0.0906 , 0.1192, and 0.1470 eV/molec., for the SEI values of 0.05, 0.1, 0.15, and 0.2 eV/molec., respectively. Note that if flow and plasma would be coupled together, this could have a negative impact on the VT-VV relaxation balance, which moves in favor of VT when the temperature increases, and this would decrease the relative contribution of N1 and N2 to the CO_2 dissociation, and hence lower the energy efficiency.

The plasma positions for highest energy efficiency for all 4 cases lie at the same position (see figure S4). The Mach number at that position is 1.83. However, higher SEI values give higher decelerations, since they add more heat (see above). According to eq. 17, the initial Mach numbers to end up with M = 1.83 are M = 3, M = 4.4, M = 6.1, and M = 12.8, respectively. A higher SEI thus requires a higher initial Mach number to counter the stronger deceleration.

The non-linear increase of the energy efficiency with increasing power (or SEI) is a result of the longer residence time. For SEI of 0.05, 0.1, 0.15, and 0.2 eV/molec., the residence time is 0.66 μs, 1.37 μs, 1.98 μs, and 2.7 μs, respectively. The residence time affects the relative contribution of the different dissociation processes, explained in more detail in section . These relative contributions are plotted in figure 9, for the four different SEI values. For SEI of 0.1, 0.15, and 0.2 eV/molec, the energetically efficient vibrationally induced dissociation processes (N1 and N2) contribute most to the overall dissociation. However, the relative contribution of N1 (with reaction enthalpy Δ H = 5.5 eV), is higher than the contribution of the most energetically favourable reaction N2 (with the lowest reaction enthalpy: Δ H = 0.35 eV). In an ideal case, these two reactions should have an equal relative contribution, so that the O atom created in N1 is used in N2.[19] The contribution of N2 increases from 26 % at SEI = 0.1 eV/molec. to 35 % at SEI = 0.2 eV/molec., which explains the higher energy efficiency (see above).

When the SEI is 0.05 eV/molec., the residence time is so short that there is not enough time for VV relaxation to populate the highest vibrational states. The dissociation is almost exclusively caused by electron impact dissociation, which is the least energy-efficient process (with Δ H = 7 eV), explaining the very low conversion and energy efficiency.

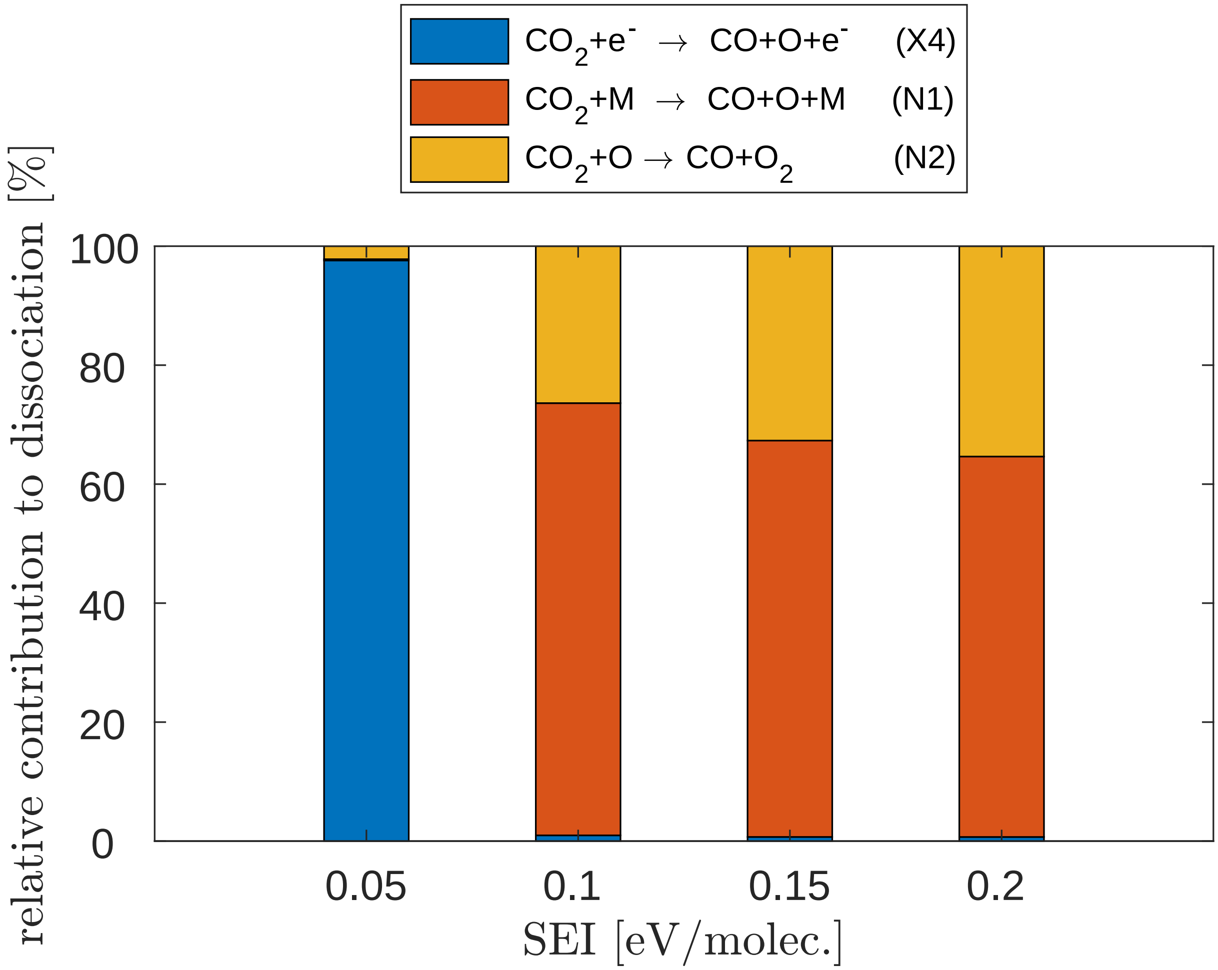

Figure 9: Relative contribution of the main CO_2 dissociation mechanisms at different SEI for the following conditions: $r_1 = 0.4$ cm, $r_2 = 2$ cm, $z_1 = 10$ cm, $p_{in} = 2$ bar, $p_{out} = 1$ bar.

Theoretical Maximum Energy Efficiency for Different Inlet and Outlet Pressures

It is clear from section , that the two main limiting factors for high energy efficiency are the short residence time of the gas in the plasma region, and the maximum deceleration heat (see eq. 17). In this section, we present the maximum calculated energy efficiency for supersonic conditions with different inlet and outlet pressures. Given that the temperature profile, used in this study, is without effect of plasma heating, and given that a higher temperature will negatively affect the energy efficiency of the system,[6] the reported efficiencies should be considered as maximum values that are achieved with this model.

The maximum heat that can be added to a certain supersonic flow is according to the criterion, described in eq. 17. This criterion is checked when applying different SEI values in the pressure drop region. The results are only taken into account if the criterion is not violated at any of the plasma starting positions. In principle, the plasma could be applied before the pressure drop, in which the pressure drop serves as cooling for the afterglow,[46] which has a benificial effect on the energy efficiency.[6] It is also important to note that the conditions used in this section represent the flow conditions, assuming that the deceleration due to the plasma has already taken place, and not the initial conditions before applying the plasma (in accordance with eq. 17). If these were initial conditions, the cases with a lower Mach flow number would have a lower allowed heat addition (see eq. 16).

Figure 10 shows the maximum energy efficiency as a function of inlet pressure, at an outlet pressure of 1 bar. The colors of the bars represent the maximum SEI that can be applied at any position in the pressure drop, without violating the above mentioned criterion of maximum deceleration heat. At lower inlet pressures, the acceleration of the flow is limited (see SI). This means that a higher SEI can be applied to the system (see eq. 17) to decelerate it from high initial Mach numbers. At higher inlet pressure, when the pressure difference between the inlet and the outlet increases, the acceleration of the flow becomes stronger, limiting the maximum SEI that can be applied to the flow. At an inlet pressure of 1.2 bar, the maximum energy efficiency is 27.4 %. As the inlet pressure increases, the maximum energy efficiency rises, until values of about 28 % are reached at inlet pressures of 1.7-2.4 bar. Note that this study is performed with stepwise increases of the SEI. Because higher energy efficiencies might exist at intermediate values of the SEI, errorbars have been added, based upon the value of the energy efficiency obtained when the criterion of eq. 17 is first broken. When the inlet pressure is further increased to 3.1 bar, the maximum energy efficiency decreases to 27.3 %, as explained below.

The initial rise of the maximum energy efficiency, when increasing the inlet pressure, can be explained by the fact that the higher Mach number in the pressure drop results in intermediate pressures that are favourable for CO_2 dissociation in MW plasmas.[2,6] The subsequent drop of the maximum energy efficiency upon further increasing the inlet pressure results from the limited SEI that can be applied in order to comply with the criterion of eq. 17, which reduces the residence time and decreases the contribution of the most energetically favourable dissociation reactions (see section and).

Figure 11 shows the maximum energy efficiency at different outlet pressures, while keeping the inlet pressure at 2 bar. At lower outlet pressures, the supersonic acceleration increases. This limits the maximum SEI that can be applied to the system (see eq. 17), and subsequently shortens the residence time and the contribution of vibrationally induced dissociation (see section and). The maximum energy efficiency also decreases with decreasing outlet pressure, since the pressure in the pressure drop region was already at optimal conditions for the case of 2 bar inlet pressure (see figure 10).

From figures 10 and 11, it is clear that the maximum energy efficiency does not increase above 30 %. However, as mentioned above, the initial Mach number should be very high in order to apply these types of SEI. In literature, energy efficiencies for MW plasmas at supersonic flow conditions have been reported, in excess of 90%.[2,9] This is clearly much higher than predicted by our models. A number of reasons could explain this mismatch:

(i) The energy efficiency strongly depends on the CO_2 dissociation upon collision with an O atom. This was studied in previous work, done by our group,[19] where it was shown that the energy efficiency depends on the activation energy of this reaction, which was significantly higher than the reaction enthalpy. However, there is a large uncertainty on the value of this activation energy. If this value would be lower, the calculated energy efficiency

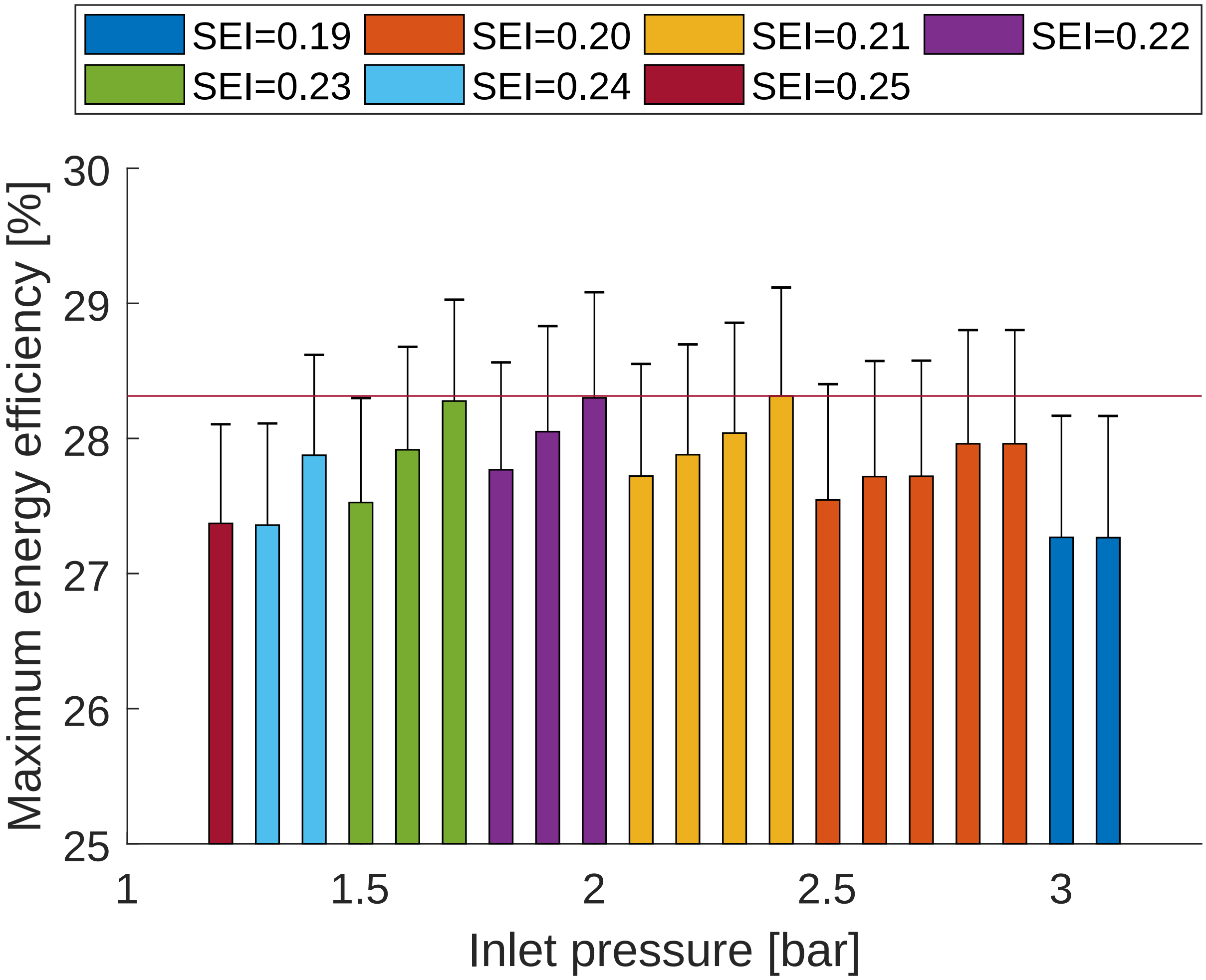

Figure 10: Maximum energy efficiencies as a function of inlet pressure, at an outlet pressure of 1 bar. The color legend gives the maximum SEI that can be applied for each case, assuming a deceleration from high Mach number flows. Errorbars have been added to take into account the stepwise increase of the SEI, because higher energy efficiencies might exist at intermediate values of the SEI (see text).

would significantly rise.[19] In addition, part of the surplus vibrational energy of CO_2, that is used to overcome this energy barrier, might be transferred to the CO vibrational levels, and subsequently redistributed to the CO_2 molecules in VV relaxation. This process is not yet taken into account in our model, but we plan to investigate the effect of it on the energy efficiency in our future work.

(ii) As stated in section , nozzle profiling could increase the maximum critical heat that can be added to the system without thermal choking. When this effect is taken into account,

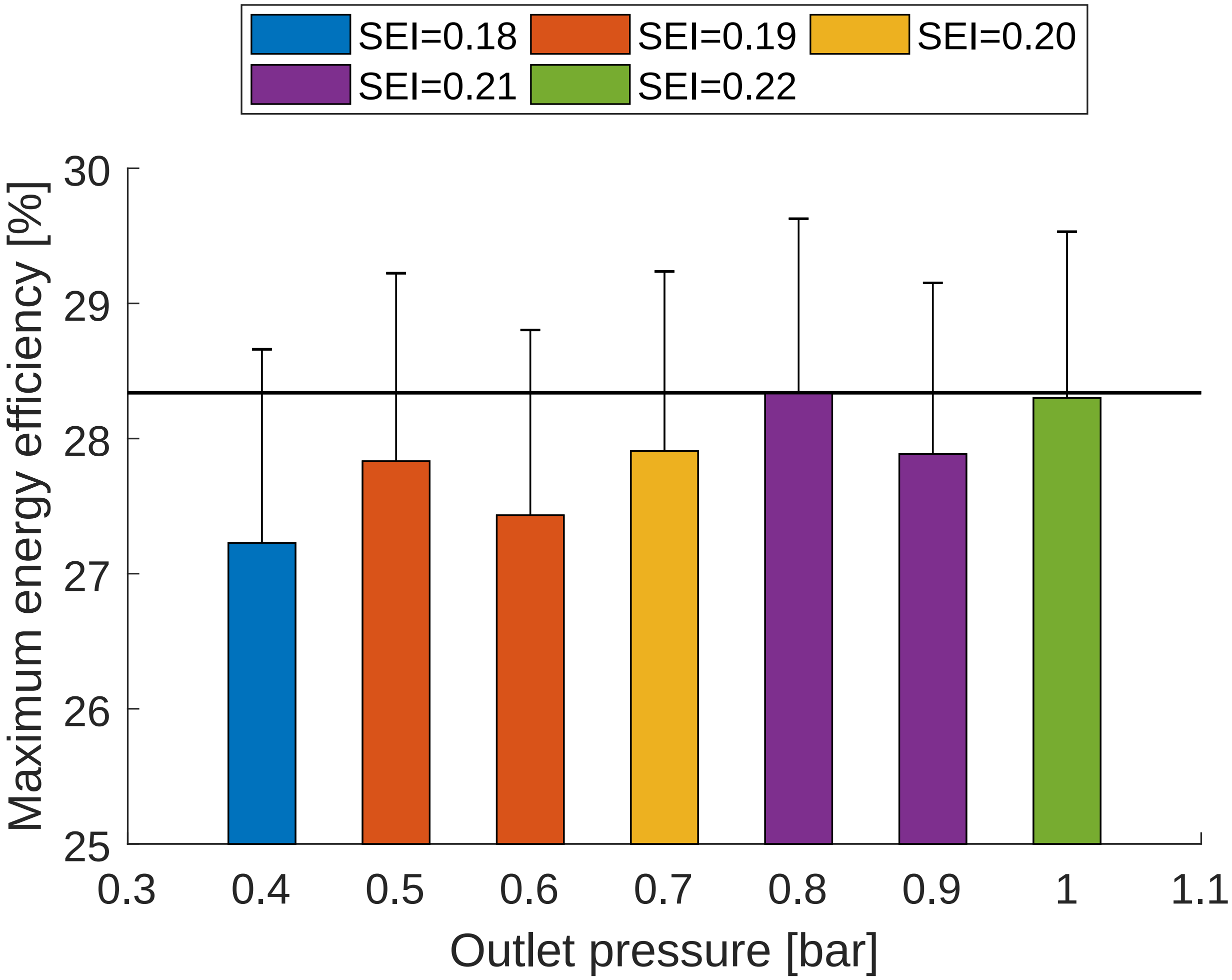

Figure 11: Maximum energy efficiency as a function of outlet pressure, at an inlet pressure of 2 bar. The color legend gives the maximum SEI that can be applied for each case, assuming a deceleration from high Mach number flows. Errorbars have been added to take into account the stepwise increase of the SEI, because higher energy efficiencies might exist at intermediate values of the SEI (see text).

it is possible to increase the amount of heat that can be added to the flow, and thus the SEI, probably resulting in a higher energy efficiency as well.

However, even when the energy efficiency would be underestimated in our model, the trends presented, and thus the message, will still be valid.

Conclusion

We developed a model, based on a combination of 2D fluid dynamics simulations of the gas flow and 0D chemical kinetics modelling of the plasma chemistry, to understand the performance of a supersonic flow microwave plasma reactor for CO_2 conversion.

Adding heat to a supersonic flow slows it down until it chokes. In this study, the plasma that was ignited meets a criterion of maximum deceleration heat, for which the supersonic flow could in theory slow down from high Mach numbers to the Mach number at which the plasma is applied. This criterion limits the SEI to values below 0.24 eV/molec.

We studied the evolution of the different reaction mechanisms through the plasma and afterglow. At the start of the plasma, electron impact vibrational excitation is the main dissociation mechanism. The model predicts that there is a spatial delay for vibrationally induced dissociation to start, due to the high velocity of the gas, combined with the time it takes for the higher vibrational levels to get sufficiently populated. Due to the limited SEI, the residence time of the gas inside the plasma region is short. As a consequence, the vibrationally induced dissociation pathway does not have enough time to operate, hence limiting the energy efficiency of the conversion process. Vibrational induced dissociation still occurs in the immediate afterglow region, due to the continued overpopulation of the higher vibrational levels, but the rate is much lower than in the plasma. The higher vibrational levels are subsequently quenched by the shockwave, which leads to a rise in pressure and temperature, after which recombination becomes more important than CO_2 dissociation.

We studied how the energy efficiency and CO_2 conversion change when moving the applied power profile (from the waveguide) through the supersonic reactor. The energy efficiency increases when the power profile moves into the pressure drop of the supersonic region. However, the most energy-efficient power position does not lie closest to the shockwave, given the continued effect of vibrationally induced dissociation in the early afterglow.

One of the main parameters to tune the energy efficiency is the outlet pressure. By changing the outlet pressure, the temperature and pressure in the supersonic region can be modified. We illustrated that for an inlet pressure of 2 bar, the maximum energy efficiency and CO_2 conversion increase with decreasing outlet pressure. This can be explained by the more optimal pressure regime for efficient CO_2 dissociation,[2,6,10] that was reached in the supersonic region at lower outlet pressures. However, the most favourable position moves further away from the position of minimum pressure.

The energy efficiency and CO_2 conversion increase upon higher input power. Indeed, the longer plasma residence time enhances the relative contribution from the most energetically favourable dissociation pathway (N1+N2), since the higher vibrational levels have more time to become populated.

Finally, we examined the maximum energy efficiency for different inlet and outlet pressures. For an outlet pressure of 1 bar, a sufficiently high inlet pressure should be applied to create favourable pressure conditions in the supersonic region. However, a too high inlet pressure will increase the Mach number, limiting the SEI that can be applied, when decelerating from high initial Mach numbers. A lower SEI results in a lower residence time, a shorter time for VV relaxation to take place, and hence a lower energy efficiency. This last phenomenon was also seen when reducing the outlet pressure, which increases the Mach number, allowing for a lower maximum SEI when coming from high initial Mach numbers, and hence a lower energy efficiency. The model predicts a maximum energy efficiency of 28.3 % at an inlet pressure of 2.4 bar, an outlet pressure of 1 bar, and a SEI of 0.21 eV/molec.

In conclusion, the model provides insight into the underlying mechanisms, as well as the limitations for the energy efficiency of supersonic MW plasmas used for CO_2 conversion. These limitations include (i) the short residence time of the gas in the plasma region, limiting the time for sufficient population of the higher vibrational levels, which is important for energy-efficient CO_2 dissociation, (ii) the shockwave, resulting in a rise in pressure and temperature, which increases the rate of recombination and quenches the higher vibrational levels from which dissociation occurs, by a rise in VT relaxation and VV ladder downclimbing, and (iii) the maximum heat, and thus power or SEI, that can be added to the supersonic flow by the plasma, to avoid thermal choking, which for CO_2 lies at 0.1867 eV/molec. In literature, much higher energy efficiencies, up to 90 %, were reported,[9] which could not be reproduced by our model. This might be caused by some inherent limitations of the 0D model, i.e. no radial contraction, or by the uncertainty on the activation energy of the most energetically efficient dissociation reaction (N2). However, even with an underestimation of the energy efficiency, the trends presented in this work, and thus the message, will still be valid.

Acknowledgement

This research was supported by the FWO project (grant G.0383.16N). The calculations were performed using the Turing HPC infrastructure at the CalcUA core facility of the Universiteit Antwerpen (UAntwerpen), a division of the Flemish Supercomputer Center VSC, funded by the Hercules Foundation, the Flemish Government (department EWI) and the UAntwerpen.

Supporting Information Available

The supporting information is available free of charge and contains:

- Reactions included in the models as well as their rate coefficients or cross sections.
- Vibrational energy transfer to the different levels.
- Flow results for different inlet and outlet conditions.
- Flow results for different Laval nozzle geometries.

References

(1) Meylan, F. D.; Moreau, V.; Erkman, S. CO_2 utilization in the perspective of industrial ecology, an overview. *Journal of CO_2 Utilization* **2015**, *12*, 101–108.

(2) Fridman, A. *Plasma chemistry*; Cambridge University Press: New York, 2008.

(3) Snoeckx, R.; Bogaerts, A. Plasma technology – a novel solution for CO 2 conversion? *Chemical Society Reviews* **2017**, *46*, 5805–5863.

(4) Kozák, T.; Bogaerts, A. Splitting of CO_2 by vibrational excitation in non-equilibrium plasmas: a reaction kinetics model. *Plasma Sources Science and Technology* **2014**, *23*, 045004.

(5) Kozák, T.; Bogaerts, A. Evaluation of the energy efficiency of CO_2 conversion in microwave discharges using a reaction kinetics model. *Plasma Sources Science and Technology* **2015**, *24*, 015024.

(6) Berthelot, A.; Bogaerts, A. Modeling of CO_2 Splitting in a Microwave Plasma: How to Improve the Conversion and Energy Efficiency. *The Journal of Physical Chemistry C* **2017**, *121*, 8236–8251.

(7) Aerts, R.; Martens, T.; Bogaerts, A. Influence of Vibrational States on CO_2 Splitting by Dielectric Barrier Discharges. *The Journal of physical chemistry C* **2012**, *116*, 23257–23273.

(8) Ponduri, S.; Becker, M. M.; Welzel, S.; Van De Sanden, M. C. M.; Loffhagen, D.; Engeln, R. Fluid modelling of CO_2 dissociation in a dielectric barrier discharge. *Journal of Applied Physics* **2016**, *119*.

(9) Asisov, R. I.; Vakar, A. K.; Jivotov, V. K.; Krotov, M. F.; Zinoviev, O. A.; Potapkin, B. V.; Rusanov, A. A.; Rusanov, V. D.; Fridman, A. A. Non-equilibrium plasma-chemical process of CO_2 decomposition in a supersonic microwave discharge. *Proceedings of the USSR Academy of Sciences* **1983**, *271*.

(10) den Harder, N.; van den Bekerom, D. C. M.; Al, R. S.; Graswinckel, M. F.; Palomares, J. M.; Peeters, F. J. J.; Ponduri, S.; Minea, T.; Bongers, W. A.; van de

Sanden, M. C. M.; van Rooij, G. J. Homogeneous CO_2 conversion by microwave plasma: Wave propagation and diagnostics. *Plasma Processes and Polymers* **2016**, 1–24.

(11) Kundu, P. K.; Cohen, I. M. *Buoyancy-Driven Exchange Flow Through Small Openings in Horizontal Partitions*; Elsevier, 1990; p 730.

(12) Peerenboom, K.; Khaji, M.; Degrez, G. Pooling through cooling: creating optimal vibrational non-equilibrium in CO_2 by supersonic expansion. *Journal of Physics D: Applied Physics* **2017**, *50*, 195201.

(13) Quaatz, J. F.; Giglmaier, M.; Hickel, S.; Adams, N. A. International Journal of Heat and Fluid Flow Large-eddy simulation of a pseudo-shock system in a Laval nozzle. *International Journal of Heat and Fluid Flow* **2014**, *49*, 108–115.

(14) Wilcox, D. C. *Turbulence Modeling for CFD*, 3rd ed.; Inc, DCW industries: US, 2006; p 522.

(15) Poinsot, T.; Veynante, D. Theoretical and Numerical Combustion. 2005.

(16) Larsson, J. Numerical Simulation of Turbulent Flows for Turbine Blade Heat Transfer Applications. Ph.D. thesis, Chalmers University of Technology, 1998.

(17) S. Pancheshnyi, B. Eismann, G.J.M. Hagelaar, L.C. Pitchford, Computer code ZDPlasKin, http://www.zdplaskin.laplace.univ-tlse.fr (University of Toulouse, LAPLACE, CNRS-UPS-INP, Toulouse, France, 2008).

(18) Berthelot, A.; Bogaerts, A. Modeling of CO 2 plasma: effect of uncertainties in the plasma chemistry. *Plasma Sources Science and Technology* **2017**, *26*, 115002.

(19) Berthelot, A.; Bogaerts, A. Pinpointing energy losses in CO 2 plasmas – Effect on CO 2 conversion. *Journal of CO2 Utilization* **2018**, *24*, 479–499.

(20) Hagelaar, G. J. M.; Pitchford, L. C. Solving the Boltzmann equation to obtain electron transport coefficients and rate coefficients for fluid models. *Plasma Sources Science and Technology* **2005**, *14*, 722–733.

(21) Phelps, A. V. Phelps Database retrieved from www.lxcat.net on September 4, 2014. http://jilawww.colorado.edu/˜avp/.

(22) Bogaerts, A.; Wang, W.; Berthelot, A.; Guerra, V. Modeling plasma-based CO_2 conversion : Crucial role of the dissociation cross section. *Plasma Sources Science and Technology* **2016**, *25*, 1–23.

(23) Berthelot, A.; Bogaerts, A. Modeling of plasma-based CO_2 conversion: lumping of the vibrational levels. *Plasma Sources Science and Technology* **2016**, *25*, 045022.

(24) Koelman, P.; Heijkers, S.; Tadayon Mousavi, S.; Graef, W.; Mihailova, D.; Kozák, T.; Bogaerts, A.; van Dijk, J. A Comprehensive Chemical Model for the Splitting of CO_2 in Non-Equilibrium Plasmas. *Plasma Processes and Polymers* **2016**, 1–20.

(25) Suzuki, I. General anharmonic force constants of carbon dioxide. *Journal of Molecular Spectroscopy* **1968**, *25*, 479–500.

(26) Herzberg, G. *Molecular Spectra and Molecular Structure: Spectra of Diatomic Molecules*; Princeton, NJ: Van Nostrand, 1950.

(27) Huber K, H. G. NIST Chemistry WebBook, NIST Standard Reference Database Number 69 Constants of Diatomic Molecules. retrieved 4 December 2013; `http://webbook.nist.gov`.

(28) Grofulović, M.; Alves, L. L.; Guerra, V. Electron-neutral scattering cross sections for CO_2: a complete and consistent set and an assessment of dissociation. *J. Phys. D: Appl. Phys.* **2016**, *49*, 395207.

(29) K. P. Huber, G. H. *Molecular Spectra and Molecular Structure IV. Constant of diatomic molecules*; Van Nostrand Rienhold Company, 1979.

(30) Pitchford, L. C. et al. LXCat : an Open-Access , Web-Based Platform for Data Needed for Modeling Low Temperature Plasmas. *Plasma Processes and Polymers* **2017**, *14*.

(31) Schwartz, R. N.; Slawsky, Z. I.; Herzfeld, K. F. Calculation of Vibrational Relaxation Times in Gases. *The Journal of Chemical Physics* **1952**, *20*, 1591.

(32) Kabouzi, Y.; Calzada, M. D.; Moisan, M.; Tran, K. C.; Trassy, C. Radial contraction of microwave-sustained plasma columns at atmospheric pressure. *Journal of Applied Physics* **2002**, *91*, 1008–1019.

(33) Shapiro, A. H. In *The Dynamics and Thermodynamics of Compressible Fluid Flow*; Sons, J. W. &., Ed.; 1953; Vol. 1; p 647.

(34) Anderson, J. D. *Modern compressible flow*; McGraw-Hill Publishing company: New York, NY, 1990; p 650.

(35) Wegener, P. P.; Cagliostro, D. J. Periodic Nozzle Flow with Heat Addition. *Combustion Science and Technology* **1973**, *6*, 269–277.

(36) Fridman, A.; Kennedy, L. A. *Plasma Physics and Engineering: Second edition*; CRC Press: Boca Raton, 2011.

(37) Bruggeman, P. J.; Sadeghi, N.; Schram, D. C.; Linss, V. Gas temperature determination from rotational lines in non-equilibrium plasmas: a review. *Plasma Sources Science and Technology* **2014**, *23*, 023001.

(38) Park, C. The Limits of Two-Temperature Kinetic Model in Air. 48th AIAA Aerospace Sciences Meeting Including the New Horizons Forum and Aerospace Exposition. Reston, Virigina, 2010; pp 1–13.

(39) Munafo, A. Vibrational State to State Kinetics in Expanding and Compressing Nitrogen Flows. *Aiaa* **2010**, 1–24.

(40) Munafò, A.; Panesi, M.; Jaffe, R. L.; Colonna, G.; Bourdon, A.; Magin, T. E. QCT-based vibrational collisional models applied to nonequilibrium nozzle flows. *The European Physical Journal D* **2012**, *66*, 188.

(41) Matsuo, K.; Miyazato, Y.; Kim, H.-d. Shock train and pseudo-shock phenomena in internal gas flows. **1999**, *35*, 33–100.

(42) Ikui, T.; Matsuo, K.; Nagai, M. The Mechanism of Pseudo-Shock Waves. *Bulletin of JSME* **1974**, *17*, 731–739.

(43) Barber, C. R. The sublimation temperature of carbon dioxide. *British Journal of Applied Physics* **1966**, *17*, 391–397.

(44) Hagena, O. F.; Obert, W. Cluster Formation in Expanding Supersonic Jets: Effect of Pressure, Temperature, Nozzle Size, and Test Gas. *The Journal of Chemical Physics* **1972**, *56*, 1793–1802.

(45) Carbone, E. A. D.; Hübner, S.; Palomares, J. M.; van der Mullen, J. J. A. M. The radial contraction of argon microwave plasmas studied by Thomson scattering. *Journal of Physics D: Applied Physics* **2012**, *45*, 345203.

(46) Goede, A. P.; Bongers, W. a.; Graswinckel, M. F.; van de Sanden, R. M.; Leins, M.; Kopecki, J.; Schulz, A.; Walker, M. Production of solar fuels by CO 2 plasmolysis. *EPJ Web of Conferences* **2014**, *79*, 01005.

Supporting Information:

Supersonic Microwave Plasma: Potential and Limitations for Energy-Efficient CO_2 Conversion

Vincent Vermeiren* and Annemie Bogaerts

Department of Chemistry, Research group PLASMANT, University of Antwerp,
Universiteitsplein 1, 2610 Antwerp, Belgium

1 List of Chemical Reactions Included in the Model

Table S1: Electron impact reactions calculated with cross sections data, using the calculated EEDF, as explained in section 2.3 of the main paper, as well as the references where the data are adopted from.

No.	Reaction	Ref	Note*
(X1)[a]	$e^- + CO_2 \rightarrow 2e^- + CO_2^+$	S1	
(X2)[b]	$e^- + CO_2 \rightarrow 2e^- + O + CO^+$	S1	
(X3)[b]	$e^- + CO_2 \rightarrow O^- + CO$	S1	
(X4)[b]	$e^- + CO_2 \rightarrow e^- + O + CO$	S1	
(X5)[a]	$e^- + CO_2 \rightarrow e^- + CO_2[e_1]$	S1	
(X6)[c]	$e^- + CO_2 \leftrightarrow e^- + CO[v_i]$	S1	i=a,b,c,d
(X7)[c]	$e^- + CO_2[v_i] \leftrightarrow e^- + CO_2[v_j]$	S1	i=0-5
(X8)[b]	$e^- + CO \rightarrow 2e^- + CO^+$	S2	
(X9)[b]	$e^- + CO \rightarrow C + O^-$	S3	
(X9bis)[b]	$e^- + CO \rightarrow e^- + C + O$	S4	
(X10)[a]	$e^- + CO \rightarrow e^- + CO[e_x]$	S4	x=1-4
(X11)[c]	$e^- + CO \rightarrow e^- + CO[v_i]$	S4	i=1-10
(X12)[b]	$e^- + O_2 \rightarrow e^- + O + O$	S5	
(X12M)[a]	$e^- + O_2 + M \rightarrow e^- + O_2^- + M$	S5	
(X13)[b]	$e^- + O_2 \rightarrow O + O^-$	S5	
(X14)[c]	$e^- + O_2 \leftrightarrow e^- + O_2[v_i]$	S5	i=1,2,3
(X15)[a]	$e^- + O_2 \leftrightarrow e^- + O_2[e_x]$	S5	x=1,2

a) Same cross section also used for CO_2v_i (i = the various vibrationally excited levels)

b) Cross section also used for CO_2v_i, modified by lowering the energy threshold by the energy of the excited state of CO_2v_i

c) Cross section for the various levels (i,j) scaled and shifted using Fridman's approximation from the $(0 \rightarrow 1)$ cross-section

* v_0 is ground state

Table S2: Electron impact reactions using analytical expressions for the rate coefficients, given in m^3/s and m^6/s, for two-body and three-body reactions, respectively, as well as the references where the data are adopted from. T_g and T_e are given in K and eV, respectively.

No.	Reaction	Rate coefficient	Reference
(E1a)	$e^- + CO_2^+ \rightarrow CO(v_1) + O$	$1 \times 10^{-11} T_e^{-0.5} T_g^{-1}$	S6,S7
(E1b)	$e^- + CO_2^+ \rightarrow C + O_2$	$1 \times 10^{-11} T_e^{-0.5} T_g^{-1}$	S8
(E2)[a]	$e^- + CO_4^+ \rightarrow CO_2 + O_2$	$1.61 \times 10^{-13} T_e^{-0.5}$	S8
(E3)	$e^- + CO^+ \rightarrow C + O$	$3.46 \times 10^{-14} T_e^{-0.48}$	S9,S10
(E4)[a]	$e^- + O + M \rightarrow O^- + M$	1×10^{-43}	S7

[a] The primary source was not accessible

Table S3: Ion-ion and ion-neutral reactions, as well as the references where the data are adopted from. The rate coefficients are given in m^3/s and m^6/s, for two-body and three-body reactions, respectively. T_g is given in K.

No.	Reaction	Rate coefficient	Reference
(I1)	$CO_2 + CO^+ \rightarrow CO_2^+ + CO$	1.0×10^{-15}	S11,S12
(I2a)[b]	$CO_2 + O^- + CO_2 \rightarrow CO_3^- + CO_2$	1.5×10^{-40}	S11,S13
(I2b)[b]	$CO_2 + O^- + CO \rightarrow CO_3^- + CO$	1.5×10^{-40}	S11,S13
(I2c)	$CO_2 + O^- + O_2 \rightarrow CO_3^- + O_2$	3.1×10^{-40}	S11,S13
(I3)	$CO_2 + O_2^- + M \rightarrow CO_4^- + M$	4.7×10^{-41}	S11,S13
(I4)	$CO + O^- \rightarrow CO_2 + e$	5.5×10^{-16}	S11,S14
(I5)	$CO + CO_3^- \rightarrow 2CO_2 + e$	5×10^{-19}	S15
(I6)[a]	$CO_3^- + CO_2^+ \rightarrow 2CO_2 v_b + O$	5×10^{-13}	S7
(I7)[a]	$CO_4^- + CO_2^+ \rightarrow 2CO_2 v_b + O_2$	5×10^{-13}	S7
(I8)[a]	$O_2^- + CO_2^+ \rightarrow CO_2 v_1 + O_2 + O$	6×10^{-13}	S7
(I9)	$CO_3^- + O \rightarrow CO_2 + O_2^-$	8×10^{-17}	S16
(I10a)[a]	$CO_4^- + O \rightarrow CO_3^- + O_2$	1.12×10^{-16}	S11
(I10b)[a]	$CO_4^- + O \rightarrow CO_2 + O_2 + O^-$	1.4×10^{-17}	S11
(I11)	$O + O^- \rightarrow O_2 + e$	2.3×10^{-16}	S17
(I12)[a]	$O + O_2^- \rightarrow O_2 + O^-$	1.5×10^{-16}	S11
(I13)	$O_2^- + M \rightarrow O_2 + M + e$	$2.7 \times 10^{-16} (\frac{T_g}{300})^{0.5} exp(-5590/T_g)$	S18,S19
(I14)[c]	$O^- + M \rightarrow O + M + e$	$2.3 \times 10^{-15} exp(-26000/T_g)$	S19–S21

[a] The primary source was not accessible

[b] The rate coefficient of $CO_2 + O^- + He \rightarrow CO_3^- + He$ was used, due to the lack of further information.

[c] For usual values of gas temperature, i.e. $T_g \ll 26000$ K, the rate coefficient is very low, as pointed out by Gudmundsson.[S22]

Table S4: Neutral-neutral reactions, as well as the references where the data are adopted from. The rate coefficients are given in m^3/s and m^6/s, for two-body and three-body reactions, respectively. T_g is given in K. The α parameter determines the effectiveness of lowering the activation energy for reactions involving vibrationally excited levels of the molecules (see details in S23,S24).

No.	Reaction	Rate coefficient	α	References
(N1)	$CO_2 + M \rightarrow CO + O + M$	$6.06 \times 10^{-16} exp(-52525/T_g)$	0.82	S25
(N2)	$CO_2 + O \rightarrow CO + O_2$	$2.8 \times 10^{-17} exp(-16400/T_g)$	0.57	S26
(N3)	$CO_2 + C \rightarrow 2CO$	$< 10^{-21}$	n.a.	S27
(N4)[a]	$CO + O + M \rightarrow CO_2 + M$	$8.3 \times 10^{-46} exp(-1510/T_g)$	0.0	S28,S29
(N5)	$O_2 + CO \rightarrow CO_2 + O$	$4.2 \times 10^{-18} exp(-24000/T_g)$	0.5	S29
(N6)	$O_2 + C \rightarrow CO + O$	$1.99 \times 10^{-16} exp(-2010/T_g)$	0.0	S30
(N7)	$O + C + M \rightarrow CO + M$	$2.14 \times 10^{-41} (\frac{T_g}{300})^{-3.08} exp(-2144/T_g)$	n.a.	S29,S31
(N8)	$O + O + M \rightarrow O_2 + M$	$5.2 \times 10^{-47} exp(900/T_g)$	n.a.	S29,S31
(N9)	$O_2 + M \rightarrow O + O + M$	$3.0 \times 10^{-12} \frac{1}{T_g} exp(-59380/T_g)$	0.0	S29,S31

[a] Multiply by 7, 3 or 12 for M= CO_2, CO or O_2 respectively.

Table S5: Neutral reactions between vibrationally excited molecules, as well as the references where the data are adopted from. The rate coefficients are given in m^3/s and m^6/s, for two-body and three-body reactions, respectively. T_g is given in K.

No.	Reaction	Rate coefficient	References
(V1)	$CO_2v_a + M \rightarrow CO_2 + M$	$7.14 \times 10^{-15} \, exp(-177 \, T_g^{-1/3} + 451 \, T_g^{-2/3})$	S32–S34
(V2a)	$CO_2v_1 + M \rightarrow CO_2v_a + M$	$4.25 \times 10^{-7} \, exp(-407 \, T_g^{-1/3} + 824 \, T_g^{-2/3})$	S34–S36
(V2b)	$CO_2v_1 + M \rightarrow CO_2v_b + M$	$8.57 \times 10^{-7} \, exp(-404 \, T_g^{-1/3} + 1096 \, T_g^{-2/3})$	S34–S36
(V2c)	$CO_2v_1 + M \rightarrow CO_2v_c + M$	$1.43 \times 10^{-7} \, exp(-252 \, T_g^{-1/3} + 685 \, T_g^{-2/3})$	S34–S36
(V3)	$COv_1 + M \rightarrow CO + M$	$1.0 \times 10^{-18} \, T_g \, exp(-150.7 \, T_g^{-1/3})$	S37
(V4)	$O_2v_1 + M \rightarrow O_2 + M$	$1.3 \times 10^{-14} \, exp(-158.7 \, T_g^{-1/3})$	S33,S34
(V5)	$CO_2v_1 + CO_2 \rightarrow CO_2v_a + CO_2v_b$	$1.06 \times 10^{-11} \, exp(-242 \, T_g^{-1/3} + 633 \, T_g^{-2/3})$	S34–S36
(V6)	$CO_2v_1 + CO_2 \rightarrow CO_2 + CO_2v_1$	$1.32 \times 10^{-18} \, (\frac{T_g}{300})^{0.5} \frac{250}{T_g}$	S38,S39
(V7)	$COv_1 + CO \rightarrow CO + COv_1$	$3.4 \times 10^{-16} (\frac{T_g}{300})^{0.5} \, (1.64 \times 10^{-6} \, T_g + \frac{1.61}{T_g})$	S40,S41
(V8)	$CO_2v_1 + CO \rightarrow CO_2 + COv_1$	$4.8 \times 10^{-12} \, exp(-153 \, T_g^{-1/3})$	S34,S35

2 Flow Results for an Inlet Pressure of 4 bar

Figure S1 shows the flow results at a higher inlet pressure than presented in the main paper, namely 4 bar, and an outlet pressure of 1 bar. The results show the formation of a third distinct region (III), called the shock train, that forms between the supersonic and the mixing region. The shock train is characterized by a sequence of shocks separating subsonic from supersonic regions.[S42] After each shock, the flow accelerates again to supersonic velocities, after which it is decelerated by the following shock. The region is characterized by pressure and temperature oscillations.

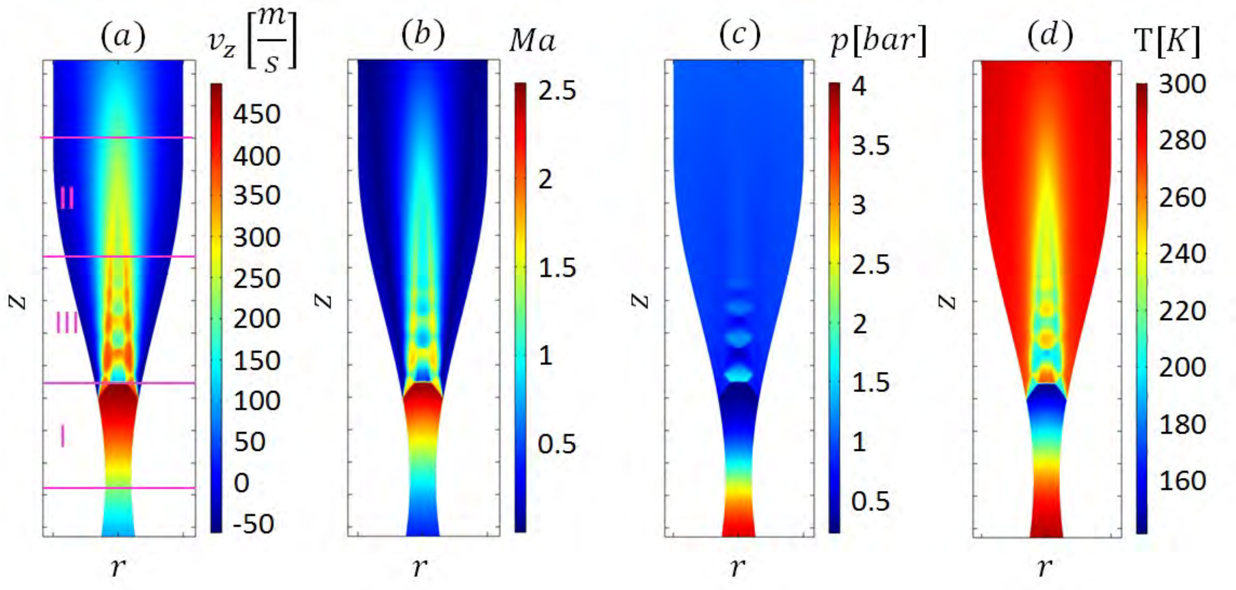

Figure S1: (a) Axial velocity magnitude, (b) Mach number, (c) static pressure and (d) static temperature in the case of $r_1 = 0.4$ cm, $r_2 = 2$ cm, $z_1 = 10$ cm, $p_{in} = 4$ bar, $p_{out} = 1$ bar.

3 Vibrational Energy Transfer

In figure 6 of the main paper, it was shown that in the beginning of the plasma, VV relaxation transports energy from the higher vibrational levels to lower vibrational levels in a ladder downclimbing process. The explanation for this lies in the fact that CO_2(V2) receives more energy from the electrons than CO_2(V1). This can be seen in figure S2, where the rate of electron energy loss to the lowest vibrational levels upon excitation from ground state CO_2 is shown. Next to the fact that more electron energy goes to the second level of the asymmetric vibrational mode instead of the first level, the density of the latter can be further depleted by electron impact vibrational excitation from that level to the higher vibrational levels.

The VV energy transfer reacts to this non-equilibrium between the first and the second vibrational level. In figure S3, it can be seen that the first vibrational level is strongly populated by VV relaxation.

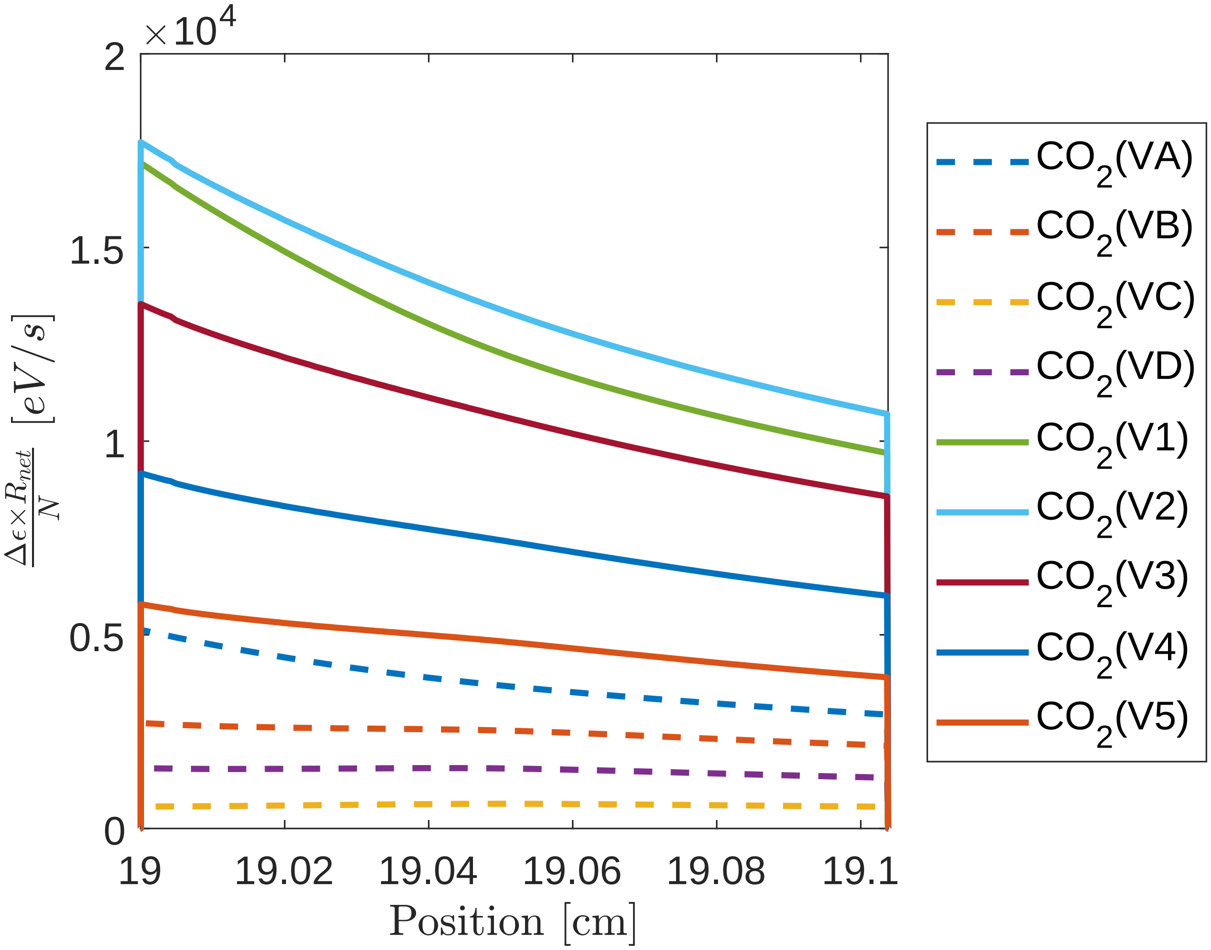

Figure S2: Electron energy loss to the different vibrational levels from ground state CO_2 inside the plasma, which ranges from z=19 to z=19.1 cm (cf. Figure 6 of the main paper), with SEI = 0.2 eV/molec. The other conditions are: $r_1 = 0.4$ cm, $r_2 = 2$ cm, $z_1 = 10$ cm, $p_{in} = 2$ bar, $p_{out} = 1$ bar

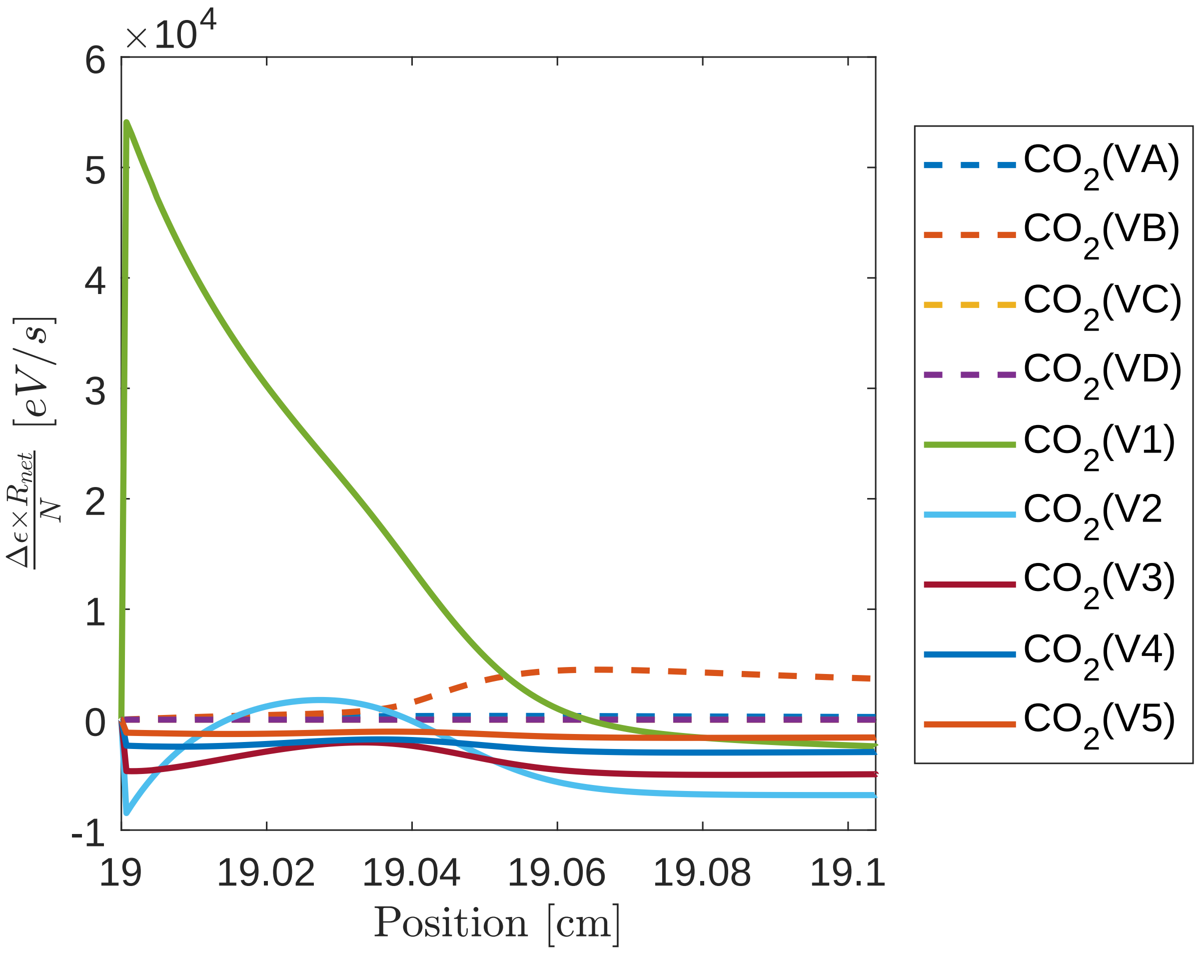

Figure S3: Energy transfer to the different levels in VV relaxation from the other levels, inside the plasma, ranging from z=19 to z=19.1 cm, with SEI = 0.2 eV/molec. The other conditions are: $r_1 = 0.4$ cm, $r_2 = 2$ cm, $z_1 = 10$ cm, $p_{in} = 2$ bar, $p_{out} = 1$ bar.

4 Effect of the Power on the Energy Efficiency

In figure S4 we show the energy efficiency and conversion as a function of the plasma position in the reactor, at three different SEI values, namely 0.05, 0.1, 0.15, and 0.2 eV/molec. The energy efficiency shows the same trend in the four different cases.

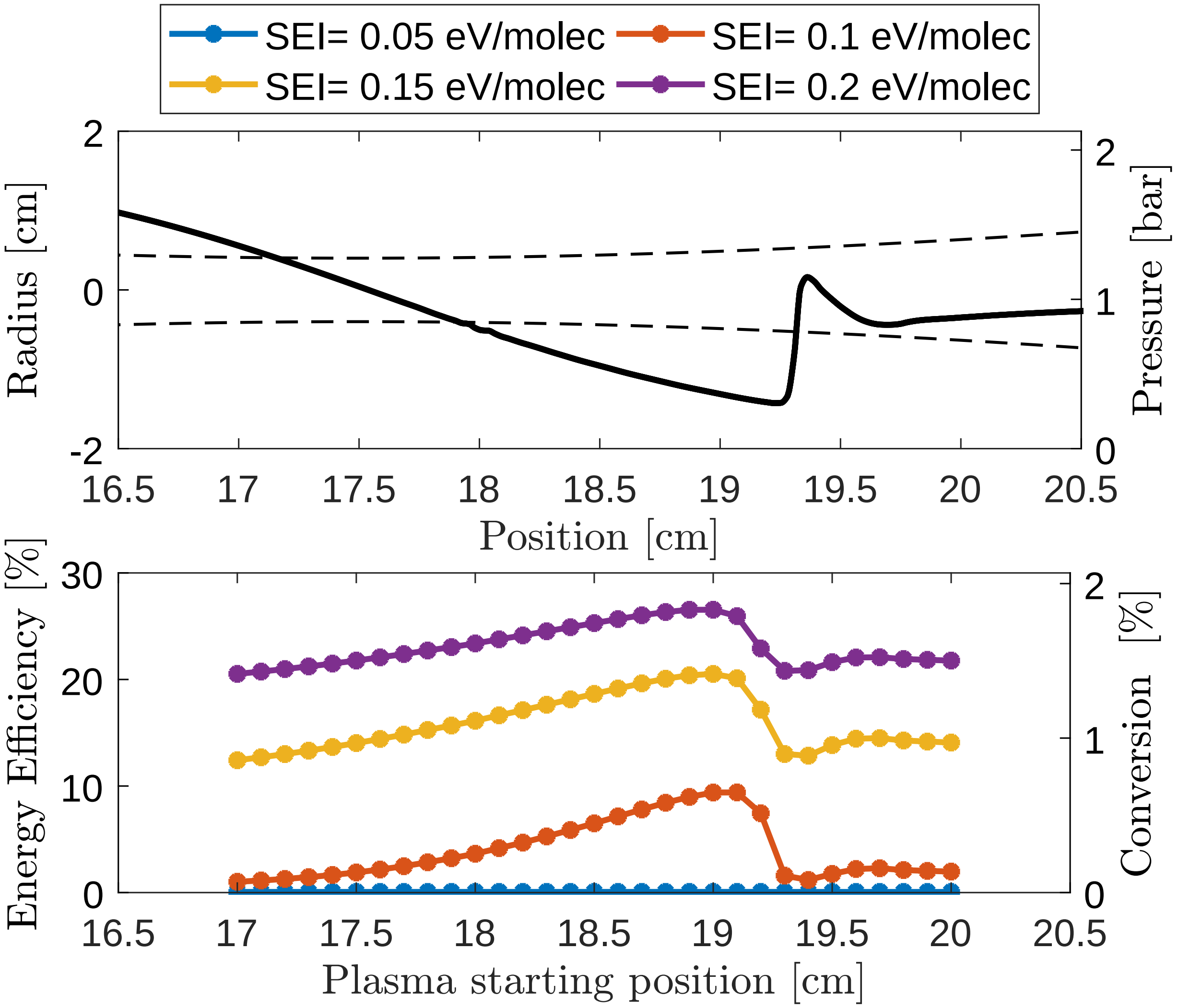

Figure S4: Conversion and energy efficiency (bottom panel) as a function of plasma position in the reactor, for four different SEI values. The other conditions are: $r_1 = 0.4$ cm, $r_2 = 2$ cm, $z_1 = 10$ cm, $p_{in} = 4$ bar, $p_{out} = 1$ bar. The radius of the reactor (dashed line) and pressure (full line) are plotted in the top panel.

5 Flow results for different inlet pressure

Figure S5 shows the evolution of the Mach number (top panel), pressure (middle panel) and temperature (bottom panel) for different inlet pressures, and an outlet pressure of 1 bar. With increasing inlet pressure, the maximum Mach number increases, and the minimum temperature decreases. In addition, the pressure minimum in the supersonic region decreases when the inlet pressure rises from 1.2 bar to 2 bar. A further increase of the inlet pressure does not change the minimum pressure, since the total pressure increases as well, requiring a higher Mach number to reach the same pressure in the supersonic region. The position of the pressure minimum, however, shifts a bit to later in the supersonic reactor.

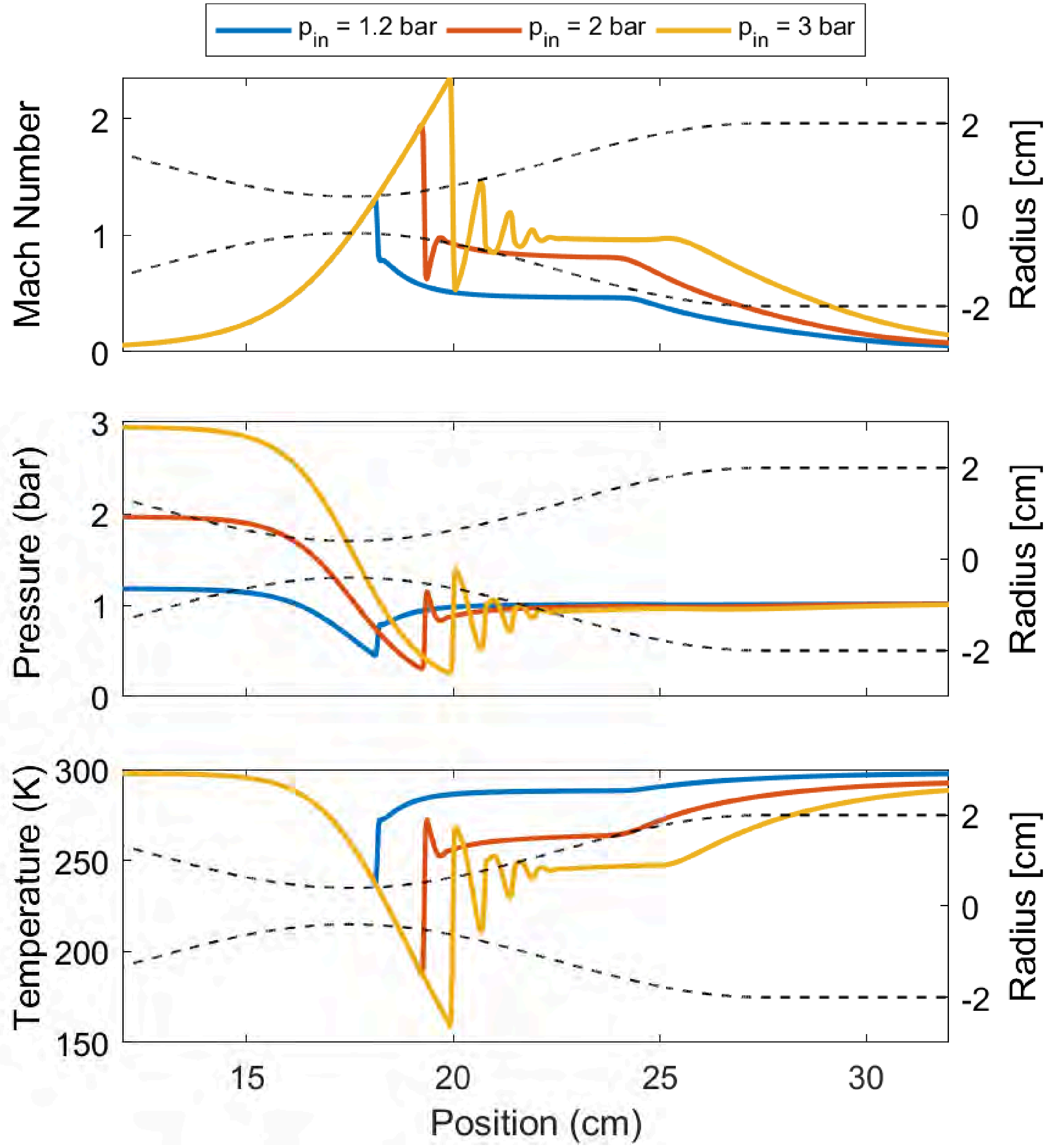

Figure S5: Mach number (top panel), pressure (middle panel) and temperature (bottom panel) as a function of position for different inlet pressures. The radius of the geometry is given in dashed lines.

6 Flow Results for Different Outlet Pressure

Figure S6 shows the evolution of the Mach number (top panel), pressure (middle panel) and temperature (bottom panel) for different outlet pressures, at an inlet pressure of 2 bar. A lower outlet pressure increases the Mach number, decreases the pressure, and decreases the temperature in the supersonic region. This makes the outlet pressure one of the main parameters to compensate for the decrease in Mach number, increase in temperature, and increase in pressure upon heat addition of the plasma.

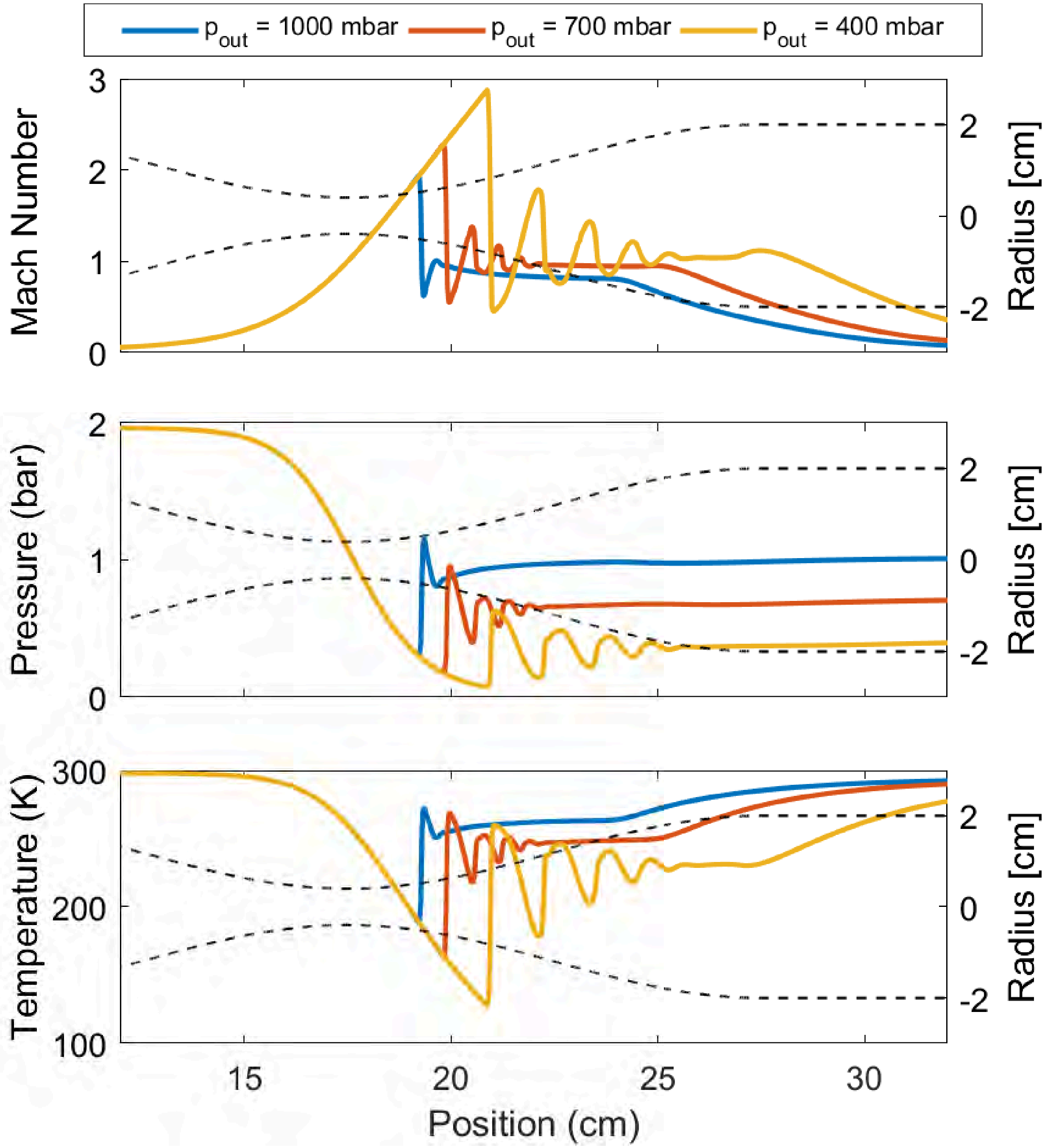

Figure S6: Mach number (top panel), pressure (middle panel) and temperature (bottom panel) as a function of position for different outlet pressures. The radius of the geometry is given in dashed lines.

7 Flow Results for Different Geometries

Figure S7 shows the evolution of the Mach number (top panel), pressure (middle panel) and temperature (bottom panel) for different values of z_1, at an inlet pressure of 2 bar and an outlet pressure of 1 bar. The supersonic region is elongated when the z_1 parameter is increased. The values of the parameters increase or decrease to the same local minima or maxima.

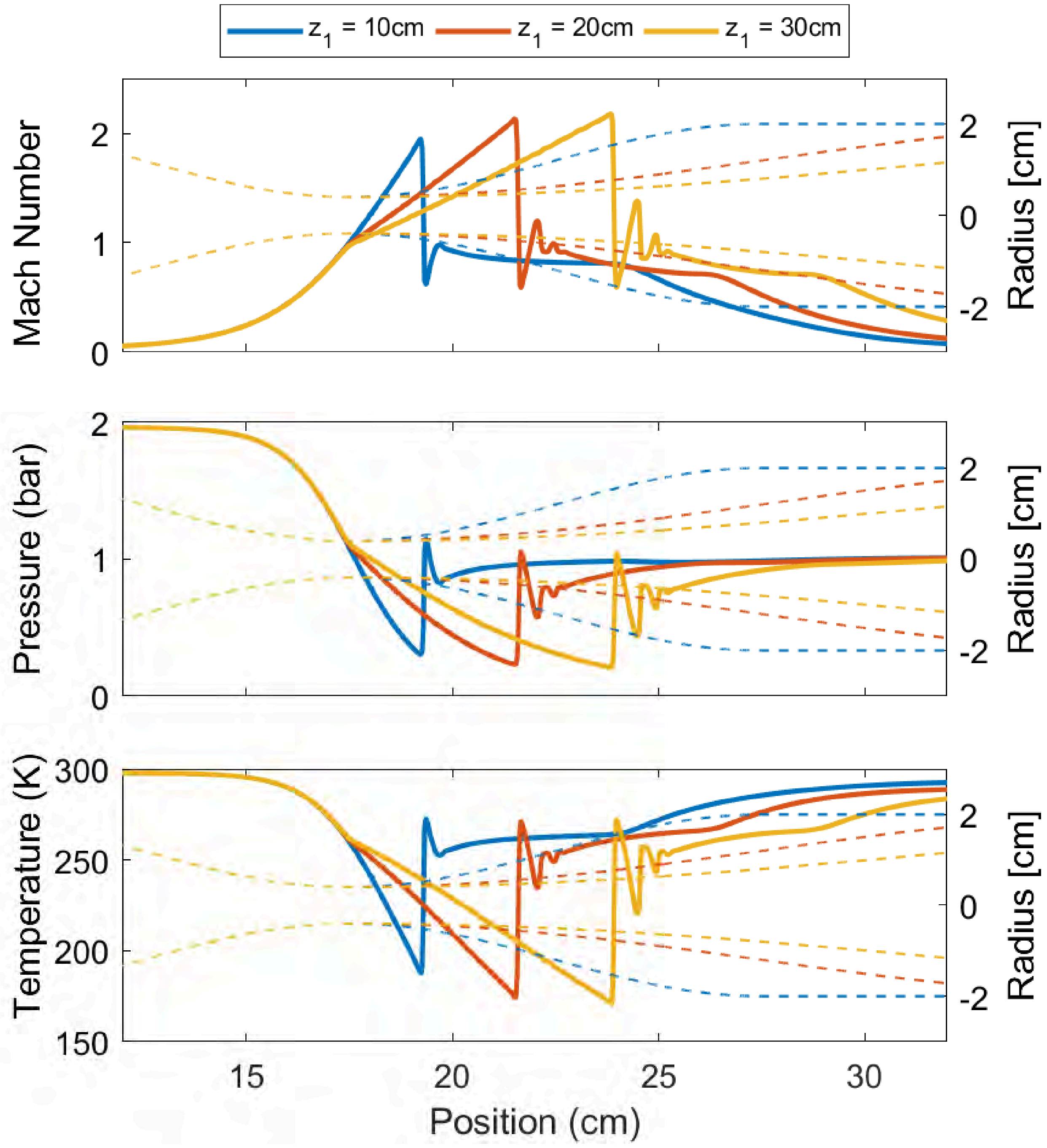

Figure S7: Mach number (top panel), pressure (middle panel) and temperature (bottom panel) as a function of position for different z_1. The radius of the geometries is given in dashed lines.

8 References

References

(S1) Phelps, A. V. Phelps Database retrieved from www.lxcat.net on September 4, 2014. http://jilawww.colorado.edu/~avp/.

(S2) Tian, C.; Vidal, C. R. Cross sections of the electron impact dissociative ionization of CO, CH_4 and C_2H_2. *Journal of Physics B: Atomic, Molecular and Optical Physics* **1998**, *31*, 895–909.

(S3) Rapp, D.; Briglia, D. D. Total Cross Sections for Ionization and Attachment in Gases by Electron Impact. II. Negative Ion Formation. *The Journal of Chemical Physics* **1965**, *43*, 1480–1489.

(S4) Land, J. E. Electron scattering cross sections for momentum transfer and inelastic excitation in carbon monoxide. *Journal of Applied Physics* **1978**, *49*, 5716–5721.

(S5) Lawton, S. A.; Phelps, A. V. Excitation of the $b^1\Sigma_g^+$ state of O_2 by low energy electrons. *The Journal of Chemical Physics* **1978**, *69*, 1055.

(S6) Weller, C. S.; Biondi, M. A. Measurements of Dissociative Recombination of CO_2^+ Ions with Electrons. *Physical Review Letters* **1967**, *19*, 59–61.

(S7) Thoenes, J.; Kurzius, S. C. *Plasma Chemistry Processes in the Closed Cycle EDL - Technical Report DRCPM-HEL-CR-79-11-VOL-1*; 1979.

(S8) Beuthe, T. G.; Chang, J.-S. Chemical Kinetic Modelling of Non-Equilibrium Ar-CO_2 Thermal Plasmas. *Japanese Journal of Applied Physics* **1997**, *36*, 4997–5002.

(S9) Mitchell, J. B. A.; Hus, H. The dissociative recombination and excitation of CO^+. *Journal of Physics B: Atomic and Molecular Physics* **1985**, *18*, 547–555.

(S10) Mcelroy, D.; Walsh, C.; Markwick, A. J.; Cordiner, M. A.; Smith, K.; Millar, T. J. The UMIST database for astrochemistry 2012. *Astronomy & Astrophysics* **2013**, *550*.

(S11) Albritton, D. Ion-neutral reaction-rate constants measured in flow reactors through 1977. *Atomic Data and Nuclear Data Tables* **1978**, *22*, 1–101.

(S12) Adams, N.; Smith, D.; Grief, D. Reactions of H_nCO^+ ions with molecules at 300 K. *International Journal of Mass Spectrometry and Ion Physics* **1978**, *26*, 405–415.

(S13) Fehsenfeld, F. C.; Ferguson, E. E. Laboratory studies of negative ion reactions with atmospheric trace constituents. *The Journal of Chemical Physics* **1974**, *61*, 3181–3193.

(S14) Mcfarland, M.; Albritton, D. L.; Fehsenfeld, F. C.; Ferguson, E. E.; Schmeltekopf, A. L. Flow-drift technique for ion mobility and ion-molecule reaction rate constant measurements. III. Negative ion reactions of O^- with CO, NO, H_2, and D_2. *Journal of Chemical Physics* **1973**, *59*, 6629–6635.

(S15) Price, D.; Moruzzi, J. Negative ion molecule reactions in CO_2 at high pressures and temperatures. *Vacuum* **1974**, *24*, 591–593.

(S16) Fehsenfeld, F. C.; Schmeltekopf, A. L.; Schiff, H. I.; Ferguson, E. E. Laboratory measurements of negative ion reactions of atmospheric interest. *Planetary and Space Science* **1967**, *15*, 373–379.

(S17) Belostotsky, S. G.; Economou, D. J.; Lopaev, D. V.; Rakhimova, T. V. Negative ion destruction by $O(^3P)$ atoms and $O_2(a^1\Delta_g)$ molecules in an oxygen plasma. *Plasma Sources Science and Technology* **2005**, *14*, 532–542.

(S18) Pack, J. L.; Phelps, A. V. Electron Attachment and Detachment. II. Mixtures of O_2 and CO_2 and of O_2 and H_2O. *The Journal of Chemical Physics* **1966**, *45*, 4316–4329.

(S19) Bortner, M. H.; Bourer, T.; Blank, C. A. *Defense Nuclear Agency Reaction Rate Handbook, Second Edition AD 763699*; 1972.

(S20) Hasted, J. B.; Smith, R. A. The Detachment of Electrons from Negative Ions. *Proceedings of the Royal Society A: Mathematical, Physical and Engineering Sciences* **1956**, *235*, 349–353.

(S21) Frommhold, L. Über verzögerte Elektronen in Elektronenlawinen, insbesondere in Sauerstoff und Luft, durch Bildung und Zerfall negativer Ionen (O^-). *Fortschritte der Physik* **1964**, *12*, 597–642.

(S22) Gudmundsson, J. T. *A critical review of the reaction set for a low pressure oxygen processing discharge RH-17-2004*; 2004.

(S23) Fridman, A. *Plasma chemistry*; Cambridge University Press: New York, 2008.

(S24) Kozák, T.; Bogaerts, A. Splitting of CO_2 by vibrational excitation in non-equilibrium plasmas: a reaction kinetics model. *Plasma Sources Science and Technology* **2014**, *23*, 045004.

(S25) Burmeister, M.; Roth, P. ARAS measurements on the thermal decomposition of CO_2 behind shock waves. *AIAA Journal* **1990**, *28*, 402–405.

(S26) Clark, T. C.; Garnett, S. H.; Kistiakowsky, G. B. Reaction of Carbon Dioxide with Atomic Oxygen and the Dissociation of Carbon Dioxide in Shock Waves. *The Journal of Chemical Physics* **1969**, *51*, 2885–2891.

(S27) Husain, D.; Young, A. N. Kinetic investigation of ground state carbon atoms, $C(2^3P_J)$. *Journal of the Chemical Society, Faraday Transactions 2* **1975**, *71*, 525.

(S28) Baldwin, R. R.; Jackson, D.; Melvin, A.; Rossiter, B. N. The second limit of hydrogen + carbon monoxide + oxygen mixtures. *International Journal of Chemical Kinetics* **1972**, *4*, 277–292.

(S29) Tsang, W.; Hampson, R. F. Chemical Kinetic Data Base for Combustion Chemistry. Part I. Methane and Related Compounds. *Journal of Physical and Chemical Reference Data* **1986**, *15*, 1087–1279.

(S30) Dean, A. J.; Davidson, D. F.; Hanson, R. K. A shock tube study of reactions of carbon atoms with hydrogen and oxygen using excimer photolysis of C_3O_2 and carbon atom atomic resonance absorption spectroscopy. *The Journal of Physical Chemistry* **1991**, *95*, 183–191.

(S31) Baulch, D. L.; Drysdale, D. D.; Duxbury, J.; Grant, S. *Evaluated Kinetic Data for High Temperature Reactions, Volume 3: Homogeneous Gas Phase Reactions of the O_2-O_3 System, the CO-O_2-H_2 System, and of the Sulphur-containing Species*; Butterworth, London, 1976.

(S32) Simpson, C. J. S. M.; Chandler, T. R. D.; Strawson, A. C. Vibrational Relaxation in CO_2 and CO_2–Ar Mixtures Studied Using a Shock Tube and a Laser–Schlieren Technique. *The Journal of Chemical Physics* **1969**, *51*, 2214–2219.

(S33) Taylor, R.; Bitterman, S. Survey of Vibrational Relaxation Data for Processes Important in the CO_2-N_2 Laser System. *Reviews of Modern Physics* **1969**, *41*, 26–47.

(S34) Blauer, J. A.; Gilmore, G. R. A survey of vibrational relaxation rate data for processes important to CO_2-N_2-H_2O infrared plume radiation. *Ultrasystems, Inc. Technical Report* **1973**, afrpl–tr–7.

(S35) Rosser, W. A.; Wood, A. D.; Gerry, E. T. Deactivation of Vibrationally Excited Carbon Dioxide (ν_3) by Collisions with Carbon Dioxide or with Nitrogen. *The Journal of Chemical Physics* **1969**, *50*, 4996–5008.

(S36) Herzfeld, K. F. Deactivation of Vibrations by Collision in the Presence of Fermi Resonance. *The Journal of Chemical Physics* **1967**, *47*, 743–752.

(S37) Capitelli, M.; Ferreira, C. M.; Gordiets, B. F.; Osipov, A. I. *Plasma kinetics in atmospheric gases*, springer s ed.; Springer Berlin Heidelberg, 2000.

(S38) Sharma, R. D. Near Resonant Vibrational Energy Transfer among Isotopes of CO_2. *Physical Review* **1969**, *177*, 102–107.

(S39) Kreutz, T. G.; O'Neill, J. A.; Flynn, G. W. Diode Laser Absorption Probe of Vibration-Vibration Energy Transfer in CO_2. *The Journal of Physical Chemistry* **1987**, *91*, 5540–5543.

(S40) DeLeon, R. L.; Rich, J. Vibrational energy exchange rates in carbon monoxide. *Chemical Physics* **1986**, *107*, 283–292.

(S41) Flament, C.; George, T.; Meister, K. A.; Tufts, J. C.; Rich, J. W.; Subramaniam, V. V.; Martin, J. P.; Piar, B.; Perrin, M. Y. Nonequilibrium vibrational kinetics of carbon monoxide at high translational mode temperatures. *Chemical Physics* **1992**, *163*, 241–262.

(S42) Matsuo, K.; Miyazato, Y.; Kim, H.-d. Shock train and pseudo-shock phenomena in internal gas flows. **1999**, *35*, 33–100.